Numerical study of steam condensation inside a long inclined flattened channel

S.M.A. Noori Rahim Abadi[1], William A. Davies III[2], Pega Hrnjak[2,3], Josua P. Meyer[1*]

[1]Department of Mechanical and Aeronautical Engineering, University of Pretoria, Pretoria, Private Box X20, Hatfield 0028, South Africa
ali.abadi@up.ac.za; josua.meyer@up.ac.za

[2]Air Conditioning and Refrigeration Center (ACRC), Department of Mechanical Science and Engineering, University of Illinois at Urbana-Champaign, Urbana, Illinois, USA
daviesi2@illinois.edu; pega@illinois.edu

[3]Creative Thermal Solutions (CTS), Inc., Urbana, Illinois, USA

[*]Corresponding author Tel.: +27 12 420 3104; Fax: +27 12 420 6632
Email address: josua.meyer@up.ac.za

Highlights

- CFD simulation of steam condensation inside flattened channel with high aspect ratio.
- The main condensation mechanism was drop-wise mode.
- Increase in inclination angle caused an increase in heat transfer coefficient.
- Performance of κ-ω sst turbulence model was better than κ-ε model.

Abstract:

In this work, condensation of steam inside a long inclined flattened channel was studied numerically. The simulated case is a flattened channel with a length of 10.7 m and a very high aspect ratio. The channel width and height are 0.0063 m and 0.214 m, respectively. The volume of fluid (VOF) multiphase flow formulation was used to present the governing equations. The flow field was assumed to be three-dimensional, unsteady and turbulent. Furthermore, the working fluid was water with constant properties at the specified saturation temperature. The effects of various parameters such as inclination angle, steam mass flux and saturation temperature on the condensation heat transfer coefficient, cooling wall temperature, and pressure drop along the channel were investigated. The present results showed very good agreement with the previous experimental work and available correlations. It was found that the increase in the inclination angle, steam mass flux and the decrease in the saturation temperature caused an increase in the heat transfer coefficient. The results also showed that the dominant mode of condensation was the drop-wise mode on the cooling wall. Furthermore, in some cases, complete condensation was observed, which caused sub-cooling in the condensate river and backflow from the exit region of the channel.

Keywords: Condensation, inclined flattened channel, heat transfer coefficient, VOF.

Nomenclature

E	Internal energy
F	Source term in the momentum equation
$\vec{g}$	Gravitational acceleration
G	Mass flux
G_b	Generation of turbulence kinetic energy due to buoyancy
G_ω	Generation of specific dissipation rate
G_k	Generation of turbulence kinetic energy due to mean velocity gradients
h	Heat transfer coefficient
h_{lv}	Latent heat of condensation
k	Thermal conductivity
k_l, k_v	Curvatures of liquid and vapour phases
L	Channel length

n Constant in Equation 17

P Pressure

ΔP Pressure drop

q'' Heat flux

r Tuning coefficient for condensation rate

S_l Condensation source term

S_v Evaporation source term

S_E Energy source term

t Time

T Temperature

T_{sat} Saturation temperature

$\vec{u}$ Velocity

Y_k Dissipation of turbulence kinetic energy due to turbulence

Y_ω Dissipation of ω due to turbulence

Greek symbols

α Volume fraction

μ Molecular viscosity

ρ Density

κ Turbulence kinetic energy

ε Turbulence energy dissipation rate

β Inclination angle

σ Surface tension

ω Specific dissipation rate

Subscripts

ave Average

eff Effective

l Liquid

L Laminar

m Mixture

sat Saturation

t Turbulent

v Vapour

wall Tube wall

1. Introduction

In-tube condensation is widely seen in many industries such as desalination, power plants and air conditioning. A thorough understanding of the condensation phenomenon would lead to an improved design of the systems. That would consequently improve system efficiency. Although circular tubes are used in the majority of applications, there are some particular cases, like air-cooled steam condensers, in which non-circular tubes such as elliptic tubes [1-3], rectangular tubes [4-6] and flattened tubes [7-9] are utilised. It has been proven that the thermal efficiency of such tubes are better when compared to conventional circular tubes under specific operating conditions [10].

In the thermal electric power generation industry, air-cooled condensors represent an alternative to wet cooling condensors. The thermal electric power generation industry rejects heat at a rate of about twice its electricity generation. The amount of heat rejected by the condensors of thermal electric power plants all over the world is therefore colossal. The efficiency of thermal electric power plants with wet cooling towers is in general higher than that of plants with air-cooled systems. However, the water consumption is enormous. In the USA, in 2010, about 45% of the total fresh water withdrawal [11] went to the wet cooling condensors of thermal electric power plants.

This high water consumption is a challenge for arid areas all over the world. For this reason, many dry-cooling systems have been installed, not only in the USA, but also in countries like Australia, Chile, New Zealand and South Africa. The world's largest air-cooled thermal electric power plant under construction is Kusile in South Africa, which will generate 4 800 MW of power. Although the efficiencies of air-cooled power plants are lower than those of wet-cooling towers, air-cooled systems have been developed to resolve the environmental impact and require zero water consumption [7]. A lot of work has been done on air-cooled condensors in the heating, ventilation and air-conditioning (HVAC) and chemical process industries, which is relevant to the air-cooled thermal electric power industry. The scale of heat transfer, geometrical size and shape normally differs with orders of magnitude.

The performance of non-circular tubes, compared to conventional circular tubes, has been investigated by some researchers [12, 13]. Wen et al. [13] performed a numerical simulation to study the condensation of R134a inside round and flattened tubes for the annular flow regime. They examined various aspect ratios of 2, 4 and 6 for the flattened tube in order to find the optimum value. The results showed that the pressure drop along the tube increased with the increase in aspect ratio, mass flow rate and vapour quality, but decreased with an increase in hydraulic diameter. They also found that the condensation heat transfer coefficient for the flattened tubes increased with an increase in aspect ratio and vapour quality. Furthermore, it was found that the average liquid film thickness decreased with an increase in aspect ratio and vapour quality. Finally, they proposed two improved correlations for the prediction of the condensation heat transfer coefficient and pressure drop inside flattened tubes. In another numerical work, Zhang et al. [14] focused on the same subject, but with different aspect ratios and two refrigerants, R134a and R410A. Similar trends and conclusions were achieved in their investigation. The results also showed that the enhancement of the condensation heat transfer coefficient in flattened tubes was greater at higher vapour qualities and mass fluxes. Furthermore, they found that the average liquid film thickness for R134a was about 40% thinner than for R410A. An experimental work was also performed by Kaew-On et al. [15] to further investigate the effect of aspect ratio on the condensation of R134a inside flattened tubes. They examined three aspect ratios of 0.72 (FT1), 3.49 (FT2), and 7.02 (FT3). The results showed that the condensation heat transfer coefficients were higher than those of round tubes, around 5–10%, 10–50%, and 200–400% for the tubes FT1, FT2 and FT3, respectively.

Besides the attempts to optimise the cross-sectional geometry of tubes, some researchers have tried to enhance the condensation heat transfer coefficient by imposing the effective changes in the operating conditions [16] and cooling surface conditions [17, 18], or by using nano-refrigerants [19].

Meyer and co-workers [20-23] conducted extensive experimentations on the condensation of R134a inside an inclined smooth tube. Their work provided a thorough understanding of condensation phenomena inside inclined smooth tubes and also a valuable database for future work. They examined various dominant parameters, such

as vapour quality, saturation temperature, refrigerant mass flux, heat flux, and tube inclination angle in their studies. They successfully captured different flow regimes for different operating conditions, and proposed an improved flow map regime that considered the inclination effect. Furthermore, they observed that there was an optimum region for the inclination angle between -30° and -15° where the condensation heat transfer coefficients were at their maximum. The optimum inclination angle was dependent on the operating conditions and corresponding flow regime. Abadi et al. [24-26] performed numerical simulations to regenerate the previous experiment of Meyer and co-workers [20-23]. They successfully proposed an efficient numerical method based on volume of fluid (VOF) multiphase flow formulations to predict the pressure drop, condensation heat transfer coefficient and flow regime inside the inclined tube. Their numerical results showed very good agreement, with less than 6% deviation compared to the experimental data. They also showed that the proposed numerical method could be efficiently used in other operating conditions and applications with lower cost and time compared to the experiments [27].

During the past years, some work has been done to investigate the condensation of steam in flattened tubes used in an air-cooled condenser (ACC) [28, 29]. Schoenfeld and Kröger [29] investigated the condensation of steam inside an elliptical tube used in ACCs. They observed that, at a particular steam flow rate, a sudden jump in the pressure drop, which is known as “flooding”, occurs. The results also showed that this flooding phenomenon has a significant effect on the thermal performance of the condenser. In another work, Owen and Kröger [30] numerically studied the water vapour flow distribution inside a large ACC. They found that the tube inlet loss coefficient was the dominant parameter in determining the flow distribution in the ACC. Their results also showed that up to 6% additional vapour flow through the primary condensers was required to prevent backflow due to the inlet loss coefficient distributions. Recently, Hrnjak and co-workers [7, 31-33] conducted experimental research on the condensation of steam inside a long, inclined flattened channel. They utilised a flattened channel with a length of 10.7 m and an aspect ratio of 38.1. They studied the effect of various parameters, such as inclination angle, mass flow rate and steam quality, on the condensation heat transfer coefficient and pressure drop. They found that the new configuration could obtain very high condensation heat transfer coefficients. This could

be attributed to the fact that drop-wise condensation happened in almost all the regions of the cooling wall. Furthermore, their acquired experimental data for the condensation heat transfer coefficients had more than 50% deviation compared to the available correlations. They claimed that the available experimental correlations were unable to predict the correct values of condensation heat transfer coefficient for their experimental case. Cheng et al. [34] studied the co-current condensation of steam inside an inclined flattened tube in an ACC using simple mathematical formulations. The main purpose of their work was to find an optimum inclination angle to prevent the system from freezing in cold weather. They investigated the effect of tube inclination, which varied from 0° to 85° on the liquid film thickness. The results showed that the liquid film thickness varied from 0.8 mm to 2.1 mm when the inclination angle changed from 0° to 85°. They concluded that the change in inclination angle had no significant advantage on increasing the anti-freezing capability of the heat exchanger.

The literature survey shows that there is no numerical work in which the effect of inclination angle on the condensation of steam inside long flattened tubes has been studied. As discussed above, this type of flattened tube is widely used in ACCs and provides very high heat transfer coefficients [7, 32, 33]. Therefore, it was the purpose of this study to numerically investigate the effect of inclination on the condensation of steam inside a long flattened channel. Thoroughly understanding this problem via numerical simulations would assist in the proper design of ACCs with low cost and time compared to the experiments. The numerical simulations were performed for the experimental case studies of Hrnjak and co-workers [7, 31-33]. The effects of various parameters, such as channel inclination angle, saturation temperature and mass flux, were investigated.

2. Problem statement

Figure 1 shows the schematic layout of the simulated case in the present study. According to the experimental setup of Kang et al. [7], the channel was divided in half in order to have flow visualisation. The simulated case is a flattened channel with a length of 10.7 m and a very high aspect ratio. The channel width and height are 0.0063 m and 0.214 m, respectively. As shown in Figure 1, only the right wall of the channel, which is made of steel, was cooled with a constant heat flux of 9.5 kW/m^2 (the imposed heat

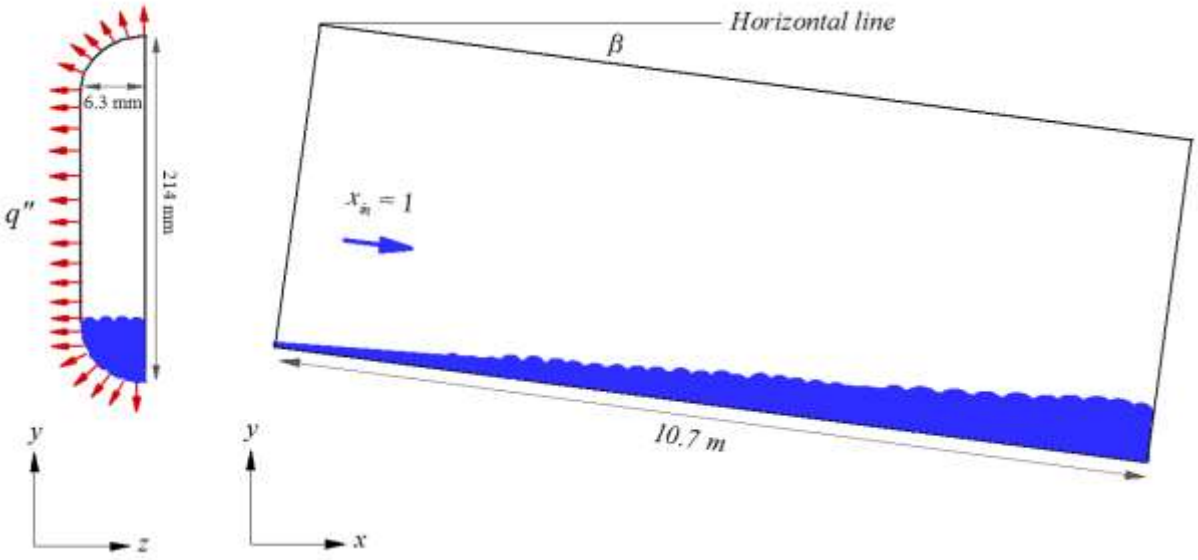

(a)

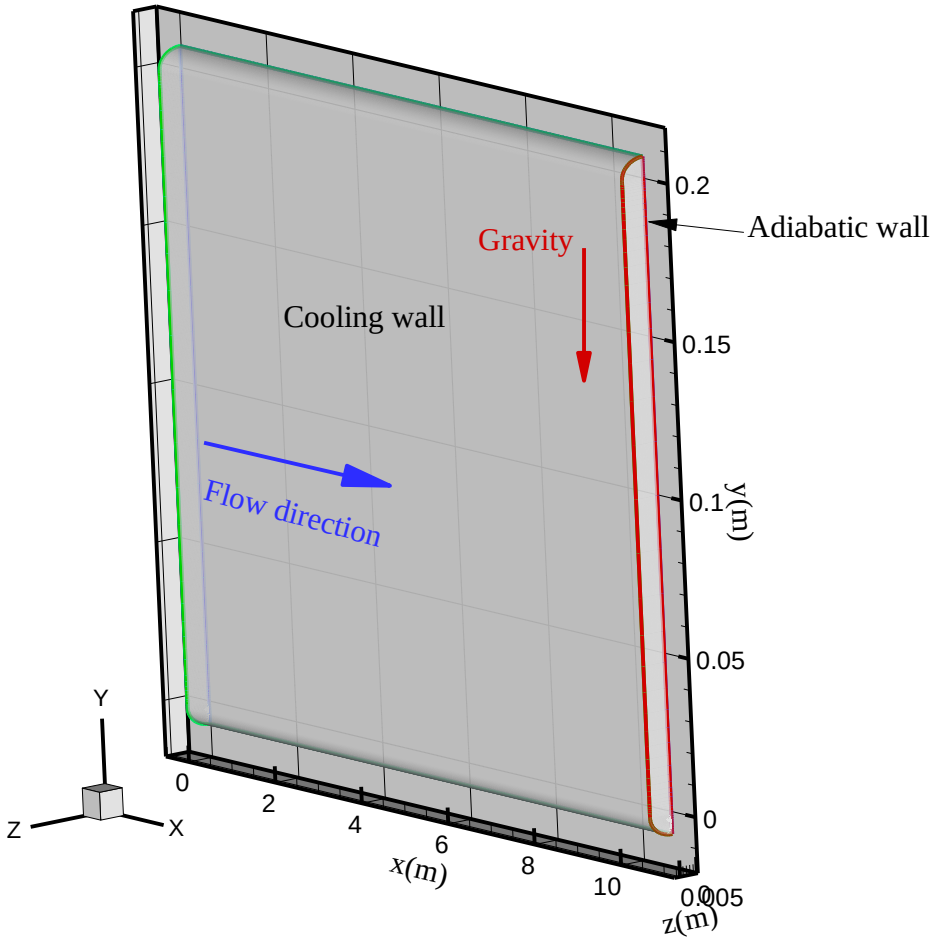

(b)

Figure 1. (a) Schematic of the present problem; (b) 3D view.

fluxes were different for the validation cases). The channel's left wall was made of polycarbonate and was maintained adiabatically. The blue in the figure represents the expected condensate river inside the channel.

Steam entered the channel with x_{in} = 1.0, $T_{in} = T_{sat} + 0.1$ (a bit in superheated condition) and a known mass flux. The inclination angle varied from β = 0.3° to β = 60°. The following assumptions were considered for the simulations:

1. According to the experimental data of Kang et al. [7], the flow regime was stratified. Therefore the VOF method could be used for the present case [25, 26].
2. The flow field was three-dimensional, unsteady and turbulent.
3. The heat flux was considered to be constant on the right wall. The experimental data showed that the value of heat flux along the *y*-coordinate changed, but it was almost constant along the *x*-coordinate [7]. In the present simulations, the variations of heat flux along the *y*-coordinate have been neglected, and it was assumed that the heat flux was constant in both directions and equalled the total value that corresponded to each experimental case.
4. The contact angle between the liquid phase and the channel right wall (steel wall) was 0°, while it was set to 82° for the left wall (the polycarbonate wall) [7, 32, 33].
5. The liquid phase (the heavier phase) was set as the primary phase and the vapour phase was set as the secondary phase [24-26].
6. Both phases were assumed to have incompressible fluids.
7. The properties of each phase were considered to be constant. Such an assumption was appropriate as the temperature variations along the channel were low.

3. Mathematical formulation

As discussed above, Kang et al. [7] observed that the flow regimes for all operating conditions were stratified or stratified-wavy. Therefore, the VOF method would be the most appropriate method for the simulation of this problem. By using this method, a sharp and clear interface between the liquid and vapour phases could be captured. The suitability of the VOF method for these types of flow regimes had already been proved [24-26, 35].

3.1. Governing equations

The governing equations in the VOF method – which consist of volume fraction for the secondary phase, continuity, mixture momentum and mixture energy equations – can be defined as follows [36]:

Vapour volume fraction:

$$\frac{\partial \rho_v \alpha_v}{\partial t} + \nabla.(\rho_v \vec{u} \alpha_v) = S_v \tag{1}$$

Continuity equation:

$$\frac{\partial \rho_m}{\partial t} + \nabla.(\rho_m \vec{u}) = 0 \tag{2}$$

Mixture momentum equation:

$$\frac{\partial (\rho_m \vec{u})}{\partial t} + \nabla.(\rho_m \vec{u}\vec{u}) = -\nabla P + \nabla.[\mu_{m,eff}(\nabla \vec{u} + (\nabla \vec{u})^T)] + \rho_m \vec{g} + \vec{F}_\sigma \tag{3}$$

Mixture energy equation:

$$\frac{\partial (\rho_m E)}{\partial t} + \nabla.[\vec{u}(\rho_m E + P)] = \nabla.(k_{m,eff} \nabla T) + S_E \tag{4}$$

Furthermore, the sum of the volume fractions of each phase in a computational cell is unity. Therefore, the final equation is presented as:

$$\alpha_l + \alpha_v = 1 \tag{5}$$

In the governing equations presented above, α is the volume fraction, and indices l and v represent the liquid and vapour phases, respectively. Moreover, u is the velocity, ρ is the density, t is the time, μ_{eff} is the effective viscosity, P is the pressure, g is the gravitational

acceleration, T is the temperature, E is the internal energy, k_{eff} is the effective thermal conductivity and F_σ is the surface tension force. Parameter S is the source term pertaining to phase changes.

In the VOF method, the average phase properties were used and were defined as follows:

$$\begin{aligned} k_m &= \alpha_l k_l + \alpha_v k_v \\ \rho_m &= \alpha_l \rho_l + \alpha_v \rho_v \\ \mu_m &= \alpha_l \mu_l + \alpha_v \mu_v \end{aligned} \tag{6}$$

Furthermore, the effective parameters μ_{eff} and k_{eff} were defined as follows:

$$\begin{aligned} \mu_{eff} &= \mu_L + \mu_t \\ k_{eff} &= k_L + k_t \end{aligned} \tag{7}$$

where the indices L and t stand for laminar and turbulent flows, respectively.

The surface tension force was calculated using the continuum surface force (CSF) model proposed by Brackbill et al. [37]:

$$F_\sigma = \sigma \frac{\alpha_l \rho_l k_v \nabla \alpha_v + \alpha_v \rho_v k_l \nabla \alpha_l}{\frac{1}{2}(\rho_v + \rho_l)} \tag{8}$$

where σ is the water surface tension. The curvatures of the vapour and liquid phases were defined as follows [37]:

$$k_l = \nabla . \frac{\nabla \alpha_l}{|\nabla \alpha_l|}, \quad k_v = \nabla . \frac{\nabla \alpha_v}{|\nabla \alpha_v|} \tag{9}$$

The flow field was turbulent as the inlet Reynolds number for the lowest mass flux, G = 6.5 kg/m^{2}s, was 7 577. In this study, two different turbulence models, *κ-ω sst* [38] and

realisable *κ-ε* [39], were examined. The governing equations of these two turbulence models were defined as follows:

κ-ω sst model [38]:

$$\frac{\partial(\rho_m k)}{\partial t}+\nabla.(\rho_m \vec{u} k)=\nabla.[(\mu_{L,m}+\frac{\mu_{t,m}}{\sigma_k})\nabla k]+G_k-Y_k \tag{10}$$

$$\frac{\partial(\rho_m \omega)}{\partial t}+\nabla.(\rho_m \vec{u} \omega)=\nabla.[(\mu_{L,m}+\frac{\mu_{t,m}}{\sigma_\omega})\nabla \omega]+G_\omega-Y_\omega \tag{11}$$

Realisable *κ-ε* model [39]:

$$\frac{\partial(\rho_m k)}{\partial t}+\nabla.(\rho_m \vec{u} k)=\nabla.[(\mu_{L,m}+\frac{\mu_{t,m}}{\sigma_k})\nabla k]+G_k+G_b-\rho_m \varepsilon \tag{12}$$

$$\frac{\partial(\rho_m \varepsilon)}{\partial t}+\nabla.(\rho_m \vec{u} \varepsilon)=\nabla.[(\mu_{L,m}+\frac{\mu_{t,m}}{\sigma_\varepsilon})\nabla \varepsilon]+\rho_m C_1 S\varepsilon-\rho_m C_2 \frac{\varepsilon^2}{k+\sqrt{\nu\varepsilon}}+C_{1\varepsilon}C_{3\varepsilon}\frac{\varepsilon}{k}G_b \tag{13}$$

$$C_1=\max[0.43,\frac{\eta}{\eta+5}],\eta=S\frac{k}{\varepsilon},S=\sqrt{2S_{ij}S_{ij}},\ S_{ij}=\frac{1}{2}(\frac{\partial \vec{u}_i}{\partial x_j}+\frac{\partial \vec{u}_j}{\partial x_i}) \tag{14}$$

where *κ*, *ε*, and ω are the turbulent kinetic energy, turbulent energy dissipation rate and specific dissipation rate, respectively. Furthermore, the terms G_k, Y_k, G_ω, Y_ω, and G_b are the generation of turbulence kinetic energy due to mean velocity gradients, dissipation of turbulence kinetic energy due to turbulence, generation of *ω*, dissipation of *ω* due to turbulence and generation of turbulence kinetic energy due to buoyancy, respectively. Further details on the constants in these two turbulence models can be found in Mentor [38, 39].

In this study, the condensation mass transfer rate is calculated based on the proposed model of Lee [40] as follows:

$$S_l=-S_v=r_l\alpha_l\rho_l\frac{T-T_{sat}}{T_{sat}}\quad T\geq T_{sat} \tag{15}$$

$$S_v = -S_l = r_v \alpha_v \rho_v \frac{T_{sat} - T}{T_{sat}} \quad T < T_{sat} \tag{16}$$

where T_{sat} is the saturation temperature of the working fluid. The coefficients r_l and r_v were tuned to fit the experimental data. The coefficients r_l and r_v may vary from 0.1 to 10^7, depending on many factors, including, but not limited to, mesh size, phase-change phenomenon, mass flow rate, computational time step size and experimental conditions [24-26]. Excessively small values of the coefficient, r, lead to a significant deviation between the interfacial and saturation temperature. However, excessively large values of r cause numerical convergence problems. In the present study, the values of r_l and r_v were considered to be equal to 8 000 s^{-1}. In order to maintain the temperature at the interfacial cells to the saturation condition, the recent development on the Lee [40] model by Shen et al. [41] was utilised. In this new model, the thermal conductivity of the mixture phase was defined as follows:

$$k_m = \alpha_l k_l + \alpha_v (\mathrm{n} \times k_v) \ \ if \ \ T < T_{sat} \tag{17}$$

where n is the tuning parameter, and can vary from 1 (classical model) to 100 [41]. By using the above correction, energy transportation within the two-phase region was enhanced and, as a result, the saturation condition at the interfacial cells, as well as the convergence of the solution process would be improved. In the present simulations, the value of n was set to 100, as the combined effect of this parameter and r lead to the lowest temperature difference of 0.6 °C between the saturation and cell temperatures at the liquid-vapour interface.

The relevant source term in the energy equation was defined as follows:

$$S_E = -S_l h_{lv} \tag{18}$$

where h_{lv} is the latent heat of condensation. The aforementioned source terms in terms of the mass and energy equations were implemented into the solver via a user-defined function.

The average heat transfer coefficient along the tube was calculated as follows:

$$h_{ave} = \frac{q''}{T_{sat} - T_{wall,ave}} \tag{19}$$

where $T_{wall,ave}$ and q'' are the average channel right wall temperature and heat flux, respectively.

3.2. Solution method

In the present study, the ANSYS FLUENT 17.1 commercial software package was used to solve the governing equations, as well as the mass transfer rate and corresponding forces. The pressure-velocity coupling was obtained using the pressure-implicit with splitting of operators (PISO) algorithm. To attain a stable solution procedure, all convective fluxes were approximated using a second-order upwind method, whereas the diffusive fluxes were discretised by central differencing. To capture the liquid-vapour interphase, the geo-reconstruct scheme was utilised. In addition, the convergence criterion was set to 10^{-5} for the residual of each parameter, and a time-step size of 10^{-4} s was used for the simulations. The simulation process continued up to t = 300 s, in which the convergence criterion was met for all simulation cases.

The following boundary conditions were set:

1. At the inlet boundary, the mass flux, temperature and quality were set.
2. The channel walls were adiabatic, except for the right wall, on which a constant heat flux was imposed. Although the value of the heat flux may vary along the tube, the experimental measurements of Kang et al. [7] showed that the variations were negligible in the axial direction. A no-slip condition was also set for all channel walls.
3. The outlet boundary condition was set as a "pressure outlet" with a gauge pressure of 0 Pa. This was set to mimic an operating condenser, which had an open-ended tube emptying into a large pipe. This differed from the experimental outlet condition, however. The experiment had a liquid trap at the outlet, forcing exit quality = 0.

4. Experimental database

The experimental facility was the one used in Kang et al. [7]. A schematic layout of the experimental facility is shown in Figure 2. The condenser tube was mounted on a hinged truss to allow measurements at downward inclination angles from 0° to 75°. Superheated steam entered the air-cooled condenser and was fully condensed so that only subcooled liquid exited the tube. Boiler power and a water-driven ejector were used to control condensation pressure and to remove non-condensable gases. The power of individual fans was also adjusted to control air velocity and profile, which provided control of condenser capacity. The facility provided measurements of steam-side pressure drop, air- and steam-side capacity, determination of steam-side heat transfer coefficient, and *in situ* visualisation of flow regimes along the entire tube length.

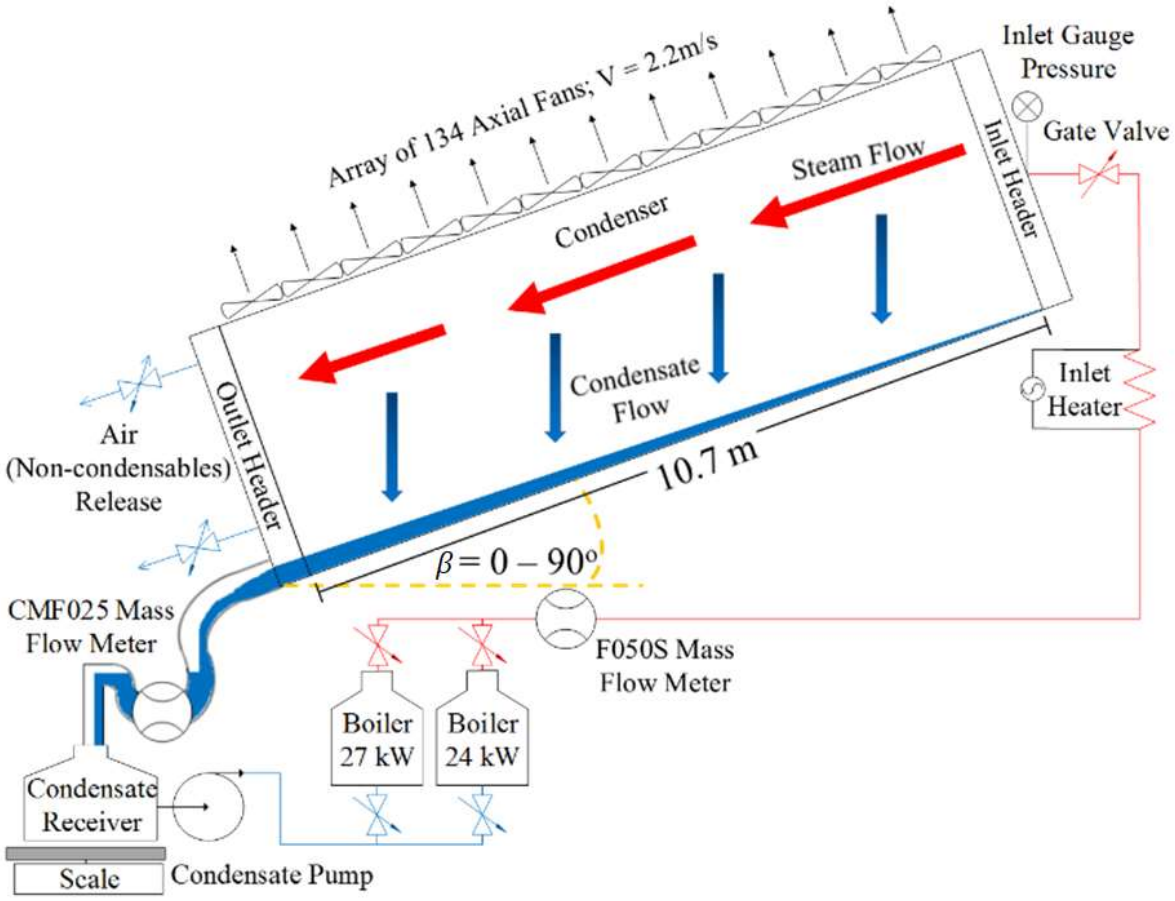

Figure 2. Diagram of experimental facility.

Visualisation was made possible by cutting the tube in half along the vertical centre line and covering the opening with a polycarbonate window, as shown in Figure 3. The polycarbonate window was held adiabatically by insulation during data-taking.

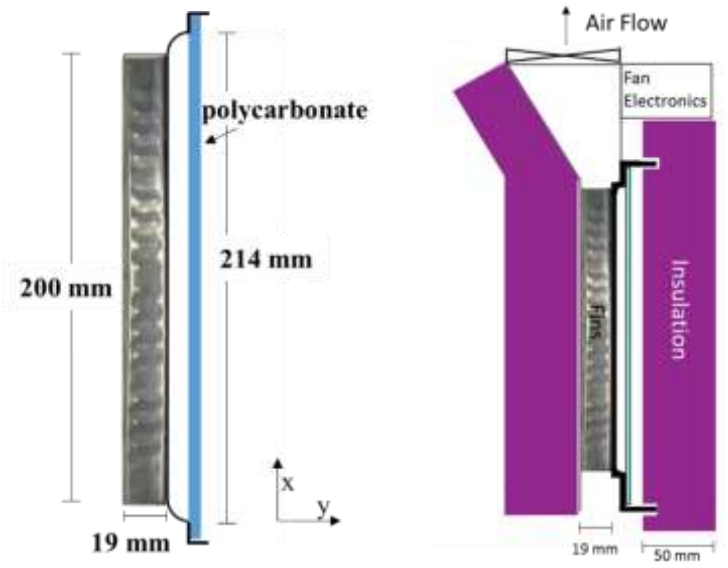

Figure 3. Half condenser tube with polycarbonate window: (a) tube stand-alone; (b) tube installed in facility.

There were two important differences between the experiment and the simulation. The experiment had a 12.5 mm diameter exit port at the bottom of the outlet header, with a vapour trap below to ensure that only liquid exited the tube. The simulation had the tube fully open to atmosphere at the outlet, which allowed an exit quality greater than zero. In this aspect, the simulation more closely resembled an operating condenser. Secondly, the experiment had a large variation in heat flux in the y-direction, due to variations in air temperature and heat transfer coefficient, as explained by Davies and Hrnjak [42]. The simulation assumed constant heat flux along the entire tube. The experiment more closely resembled an operating condenser in this aspect. Overall, the facility was designed to mimic a real-life condenser and to evaluate the effect of inclination on condenser performance. This method de-emphasised the determination of condensation heat transfer coefficient, leading to a large experimental uncertainty. Although heat flux, wall temperatures and steam temperatures were measured, the non-uniform wall temperature, heat flux and heat transfer coefficients (both air- and

steam-side) prevented the direct determination of heat transfer coefficient. Therefore, a model was made of the condensation heat transfer coefficient [43], and the model was calibrated to match the experimental results. This provided the experimental heat transfer coefficient. The error in determining heat transfer coefficient was 20%. The main causes of uncertainty were the small ΔT between the wall and the steam, and the uncertainty in the heat transfer coefficient profile near the top of the tube. In experiments at atmospheric pressure and varied inclination angles, condensation heat transfer coefficient was found to be constant along the condenser length, within the limits of uncertainty

5. Results and discussion

5.1. Validation of the numerical method

Figure 4 illustrates close-up views of the computational grids used in the present simulations. The utilised mesh was a structured grid with hexahedral cells.

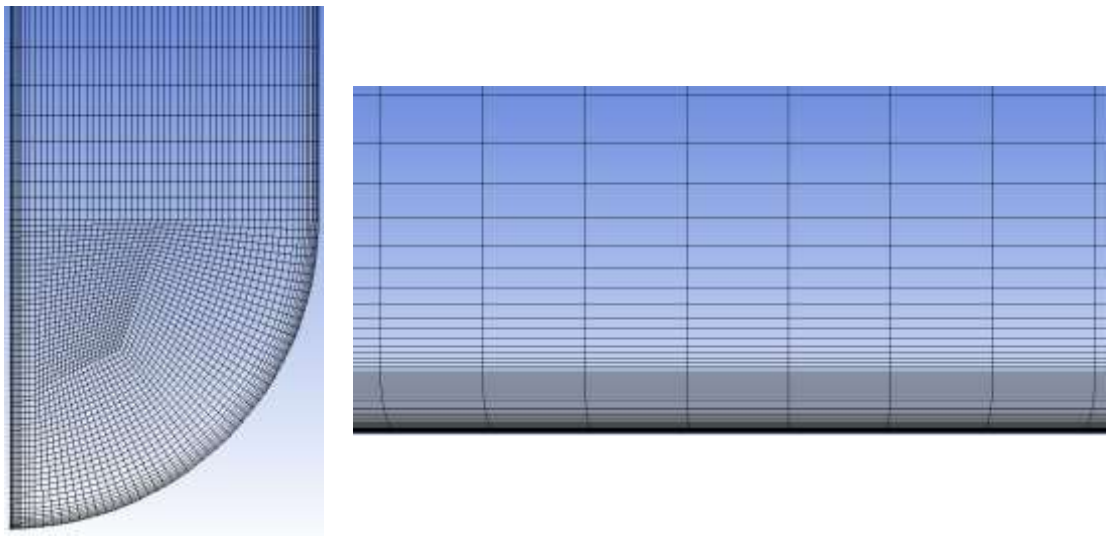

(a) (b)

Figure 4. Computational grid used in this study: (a) entrance and outlet boundaries; (b) cooling wall.

In order to assure that the grid size had no significant effect on the solution, different grid resolutions were examined. Figure 5 shows the condensation heat transfer coefficient and pressure drop along the channel for different grid sizes. The simulation case was for G = 8.5 kg/m²s, β = 0.3° and T_{sat} = 100 °C for various grid sizes. Based on

the grid study results (Figure 5), a computational grid with 6 687 500 cells was used for all simulation cases in the present study.

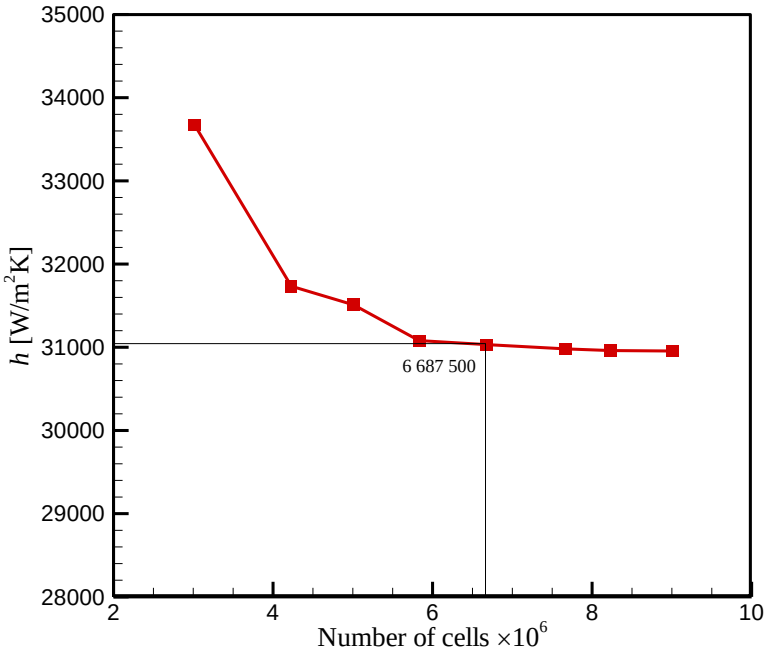

Figure 5. Variations of the average condensation heat transfer coefficient for G = 8.5 kg/m²s, β = 0.3° and T_{sat} = 100 °C for different grid sizes.

In order to validate the numerical results, the measured experimental data, discussed in section 4, was used. Figure 6 shows a comparison between the numerical results and the experimental measurement for the local heat transfer coefficient along the tube length for β = 60°, G = 8.5 kg/m²s and T_{sat} = 100 °C.

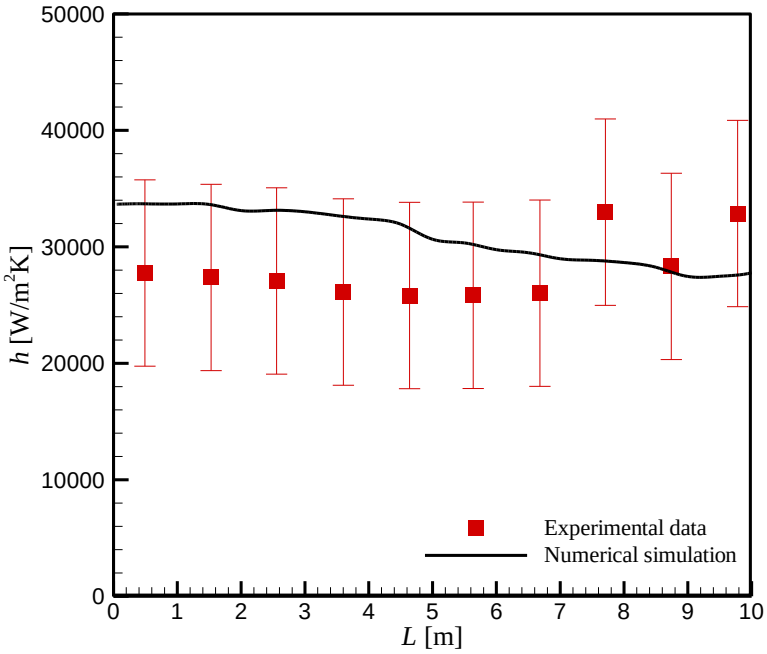

Figure 6. Comparison between the numerical results and the experimental measurements for the local condensation heat transfer coefficients along the channel length for β = 60°, G = 8.5 kg/m²s, and T_{sat} = 100 °C.

Table 1. Comparison between the present numerical results and the experimental data of Davies et al. [32] for the average condensation heat transfer coefficients at different operating conditions.

	G (kg/m²s)	$h_{ave,\,num}$ (W/m²K)		$h_{ave,\,exp}$ (W/m²K)	Deviation (%)	
		κ-ε	κ-ω *sst*		κ-ε	κ-ω *sst*
β = 0° q'' = 10.9 kW/m² T_{sat} = 100 °C	7.5	31 056	29 840	27 600	12.5	8.1
β = 0.3° q'' = 9.0 kW/m² T_{sat} = 100 °C	6.5	29 841	26594	31 500	5.2	15.5
β = 17° q'' = 9.75 kW/m² T_{sat} = 100 °C	7.5	33 789	32 010	31 200	8.3	2.6
β = 30° q'' = 12.0 kW/m² T_{sat} = 100 °C	8.5	38 941	36 547	32 300	20.5	13.1
β = 60° q'' = 12.1 kW/m² T_{sat} = 100 °C	8.5	39 125	35 874	28 700	36.3	25

Table 1 presents a comparison of the numerical results and the measured data of Davies et al. [32] for the condensation heat transfer coefficients. The values of the heat flux in the experimental work were not the same for each case. This could be due to the fact that only the cooling air velocity and temperature were fixed. Therefore, the air-side heat transfer coefficient and the resulting heat flux might change as the steam mass flux and the inclination angle change. As can be seen in Table 1, the numerical results using the κ-ω *sst* turbulence model have better accuracy compared to the κ-ε model. This might be due to the fact that the Reynolds numbers are very low, especially when the vapour phase condenses almost completely. Therefore, in the present study, the κ-ω *sst* turbulence model was used for all the simulation cases. It should also be noted that the value of y^+ varies between 1 and 2 for all simulation cases, therefore the applicability of the κ-ω *sst* turbulence model was justifiable.

Figure 7 shows the comparison between the numerical results and predicted values based on the well-known Lockhart and Martinelli [44] method for frictional pressure drops at horizontal orientation and T_{sat} = 100 °C. The results clearly show that the present numerical simulations have acceptable agreement with the correlation data. The maximum deviation for the pressure drop is 5.5%.

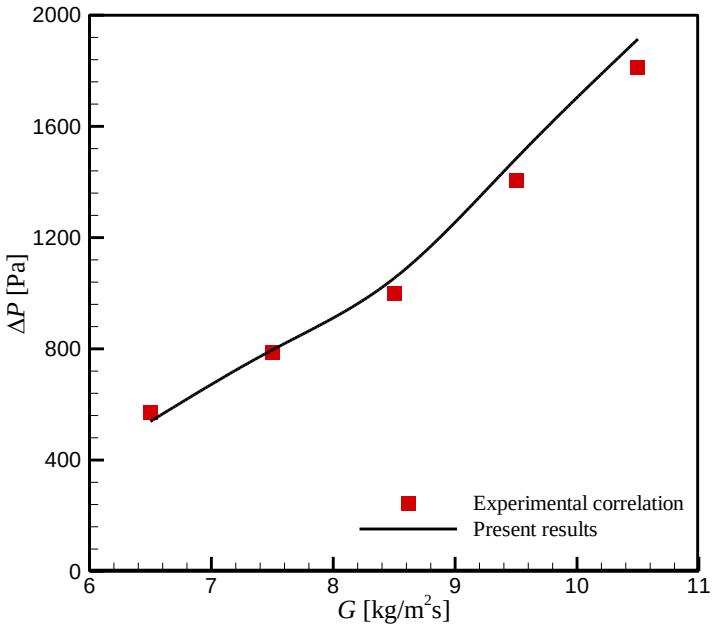

Figure 7. Comparison between the present numerical results and the correlation of Lockhart and Martinelli [44] for frictional pressure drops at a horizontal orientation.

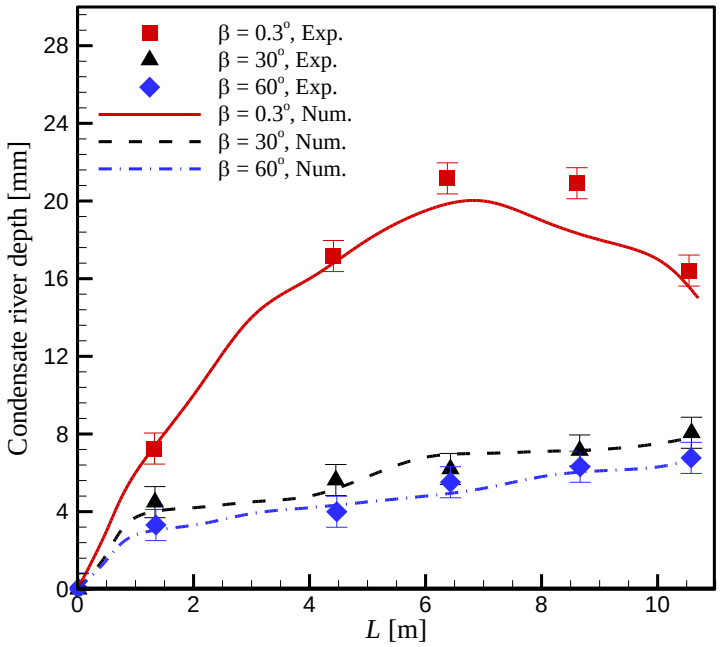

Figure 8. Comparison between the numerical results and experimental data of Kang et al. [7] for the depth of the condensate river for G = 6.5 kg/m²s and T_{sat} = 100 °C, and different channel inclination angles.

Figure 8 shows the comparison between the numerical results and experimental data of Kang et al. [7] for the depth of the condensate river for G = 6.5 kg/m²s, T_{sat} = 100 °C and different channel inclination angles. The results show that the present numerical method can successfully predict the depth of the condensate river, which means that the condensation mass transfer rate and governing forces were correctly calculated. The interesting point in Figure 8 is that the depth of the condensate river increased for all cases except for β = 0.3°. This could be attributed to the fact that, for this condition, there was a complete condensation of steam, and as a result, the mass flow rate of steam inside the channel reached zero, which caused a backflow from the exit section of the channel. The effect of the backflow on the direction of mainstream flow caused a decrease in the depth of the condensate river. This decrease in river depth was also observed in the previous experimental study of Kang et al. [7]. It is also worth mentioning that, in reality, there is always a small amount of steam inside the channel due to continuity.

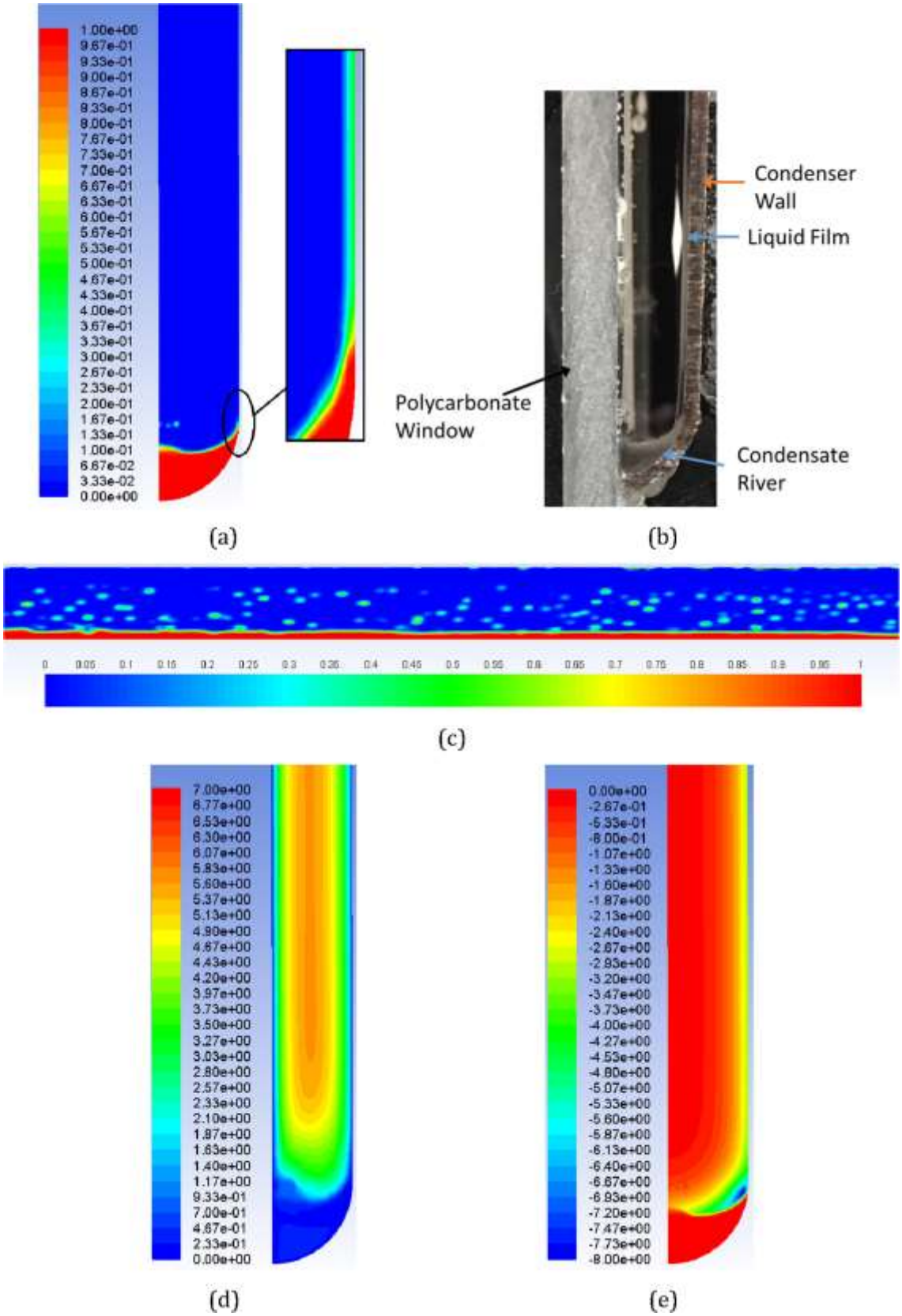

Figure 9. Variations of flow field parameters for G = 10.5 kg/m^{2}s, β = 0.3° and T_{sat} = 100 °C: (a) liquid volume fraction at x = 10.7 m; (b) experimental photo for the adiabatic case [32]; (c) liquid volume fraction at the cooling wall for 6 < x < 8 m; (d) velocity in m/s at x = 10.7 m; and (e) condensation rate in kg/m^{3}s at x = 10.7 m.

5.2. Condensing flow field parameters

The distribution of flow field parameters, such as volume fraction, pressure, temperature and heat transfer coefficient of condensing flow inside the test channel for G = 10.5 kg/m^{2}s, β = 0.3° and T_{sat} = 100 °C are presented In this section. Figure 9 shows the distribution of the liquid volume fraction (figures 9(a) and 9(b)), temperature and condensation mass transfer rate at the outlet section of the channel. As can be seen, the shape of the interface is correctly calculated by the numerical simulation. The liquid/vapour interface stretches a bit toward the y-coordinate on the right wall, which means that this wall has a wetting surface. On the other hand, the liquid/vapour interface is almost perpendicular to the polycarbonate wall. As shown in Figure 9(c), the main condensation mechanism is a drop-wise mode. This matches the condensation pattern observed experimentally [32]. In this mechanism, small droplets produced on the cooling wall fall to the bottom of the channel due to the gravitational force and form a condensate river. Due to the existence of drop-wise condensation inside the channel, the condensation heat transfer coefficients were very high compared to the conventional round tubes. In Figure 9(d), the contour of velocity is shown. The velocity was much higher in the vapour phase compared to the liquid phase due to the lower density. The condensation mass transfer rate is also shown in Figure 9(e). The mass transfer rate was the highest at the cooling wall surface, and gradually decreased toward the channel centre. Furthermore, it can be seen that no mass transfer occurs inside the condensate river, which means that the imposed heat flux in this region only caused a decrease in the liquid temperature.

The variations of the liquid volume fraction along the *y*-coordinate at different sections of the channel are shown in Figure 10. The liquid volume fraction gradually increased along the channel length due the condensation, which meant that the depth of the condensate river increased. Furthermore, the liquid volume fraction decreased rapidly along the *y*-coordinate. The contours of the liquid volume fraction clearly show that there is one wetting surface (right wall) and one non-wetting surface (left wall). They also illustrate that the depth of the condensate river increased along the channel length.

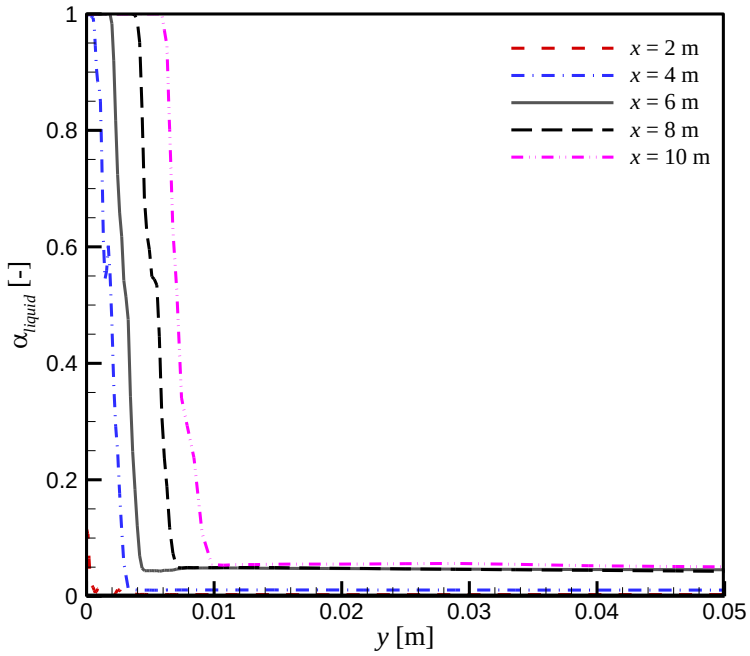

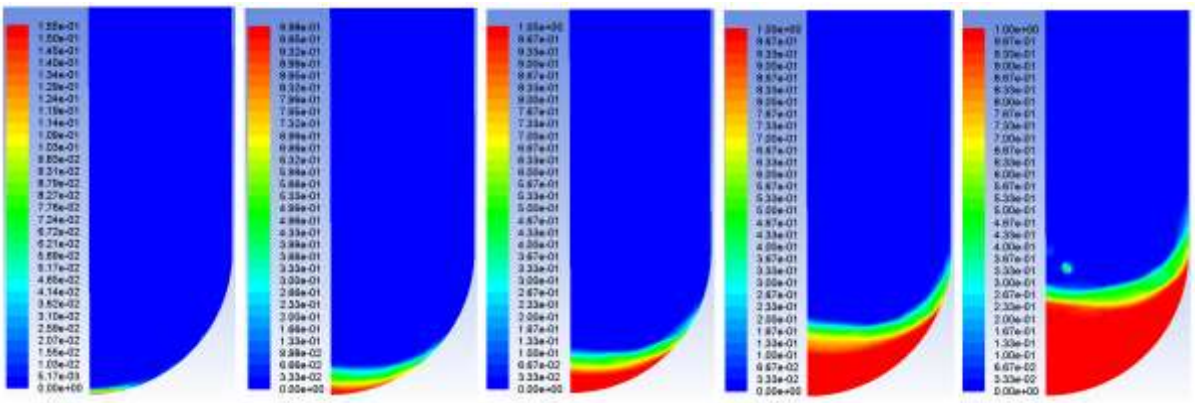

x = 2 m x = 4 m x = 6 m x = 8 m x = 10 m

Figure 10. Distributions of the liquid volume fraction along the channel length for G = 10.5

The variations in the difference between the right channel wall and the saturation temperatures along the channel length and y-coordinate are illustrated in Figure 11. At x = 2 m, the depth of the condensate river was very low. Therefore, almost all the imposed heat flux caused the mass transfer from the vapour phase to the liquid phase. Therefore the wall temperature almost equalled the saturation temperature. With the increase in x, the condensate depth increased and formed a barrier to the heat flux, and caused the decrease in the mass transfer rate, which consequently resulted in a decrease in the wall temperature. The wall temperature was almost equal to the

saturation temperature at higher values of y, because at this region, the liquid film thickness is very low.

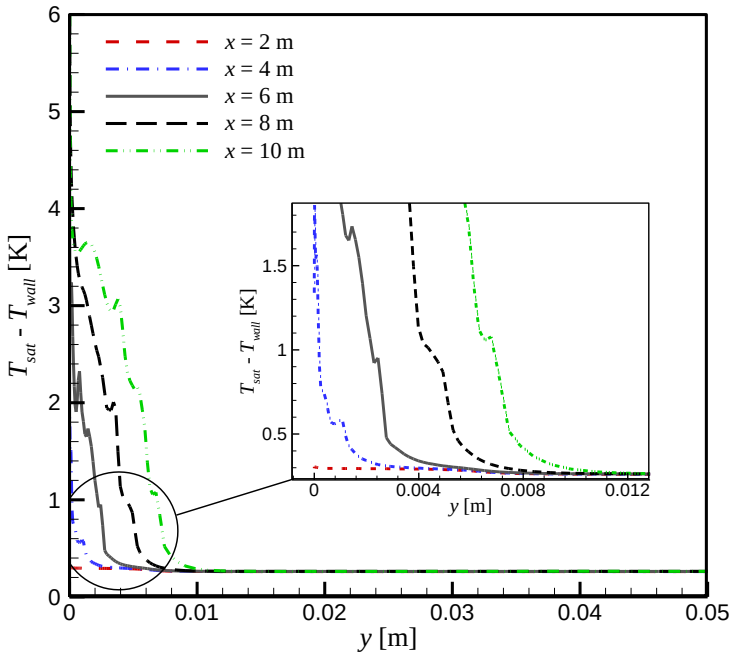

Figure 11. Variations of the channel right wall temperature along the y-coordinate for G = 10.5 kg/m^{2}s, β = 0.3° and T_{sat} = 100 °C.

The variations of the local heat transfer coefficient along the y-coordinate for different sections are shown in Figure 12. The condensation heat transfer coefficient was at its maximum at the upper part of the cooling wall where drop-wise condensation occurred. It decreased rapidly from the upper part of the channel to the condensation river. Inside the condensate river, the heat transfer mechanism was single-phase convection, and as a result, the heat transfer coefficient was very low compared to the upper part of the cooling wall. As the depth of the condensate river increased along the channel length, the portion of heat transfer on the cooling wall with the single-phase mechanism increased, therefore the average condensation heat transfer coefficient decreased along the channel length.

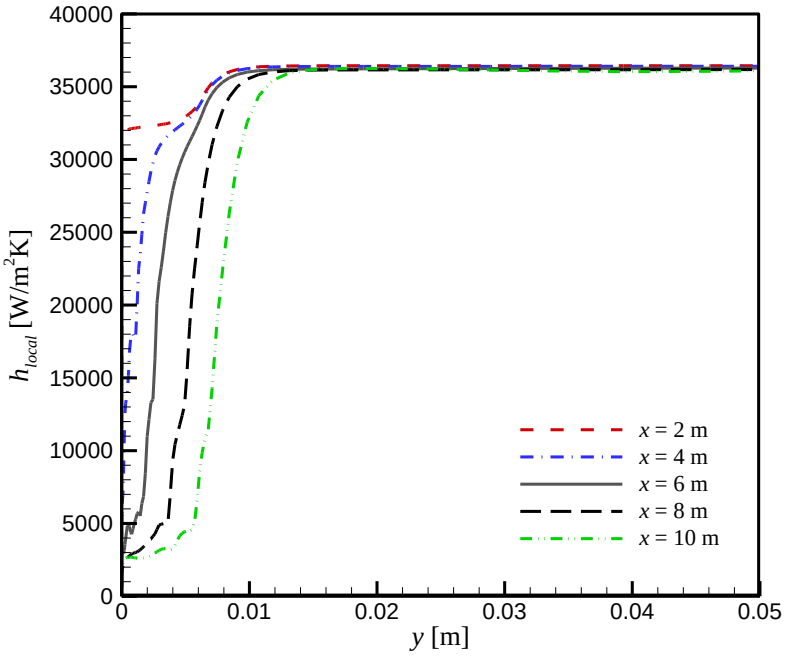

Figure 12. Distributions of the local condensation heat transfer coefficient along the y-coordinate for G = 10.5 kg/m^{2}s, β = 0.3° and T_{sat} = 100 °C.

Figure 13 shows the variations of the condensation heat transfer coefficient and pressure along the channel length. The condensation heat transfer coefficient remained almost unchanged at the entrance region of the channel. At this region, the condensation mechanism was mainly drop-wise. The volumes of the produced droplets were very small, and the larger droplets fell on the bottom of the channel. Therefore, the liquid film thickness did not change considerably. As the condensation continued along the channel, the liquid film thickness on the cooling wall and at the bottom of the channel increased. As a result, the resistance to the heat flux increased, which consequently decreased the condensation heat transfer coefficient. The value of pressure decreased along the channel due to the friction losses and reached zero at the outlet section of the channel, as had already been set for this boundary. The slope of the decreasing pressure gradually decreased along the channel length, because the mass flux of the vapour phase decreased due to the condensation phenomenon, which caused a lower pressure drop. It is interesting to note that the modelled pressure drop is higher than the experimental pressure drop, due to the outlet condition. In the model (as in an operating condenser), the exit quality was greater than zero, resulting in higher overall vapour velocity and

higher pressure drop than in the experiment. In the experiment, all of the vapour was condensed in the tube. In addition, in the experimental tube all vapour was trapped inside the tube, while in the model vapour was permitted to exit freely. Therefore, momentum pressure recovery was likely present in the experiment but not the model.

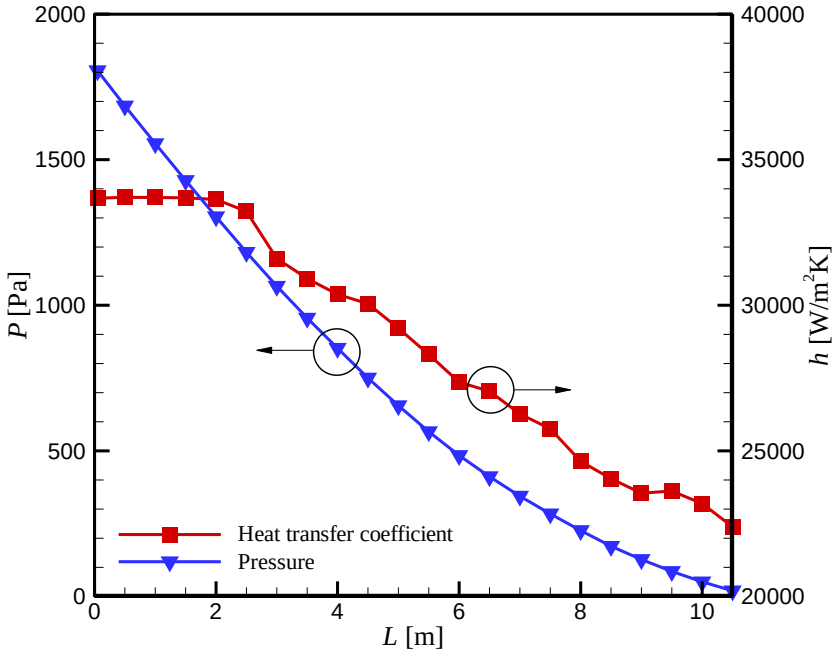

Figure 13. Variations of the pressure and condensation heat transfer coefficient along the channel length for G = 10.5 kg/m^{2}s, β = 0.3° and T_{sat} = 100 °C.

5.3. Effect of inclination angle

Figure 14 shows the effect of the channel inclination angle on the distributions of the condensation river and velocity at the outlet region of the channel for G = 6.5 kg/m^{2}s and T_{sat} = 100 °C. The increase in the inclination angle caused a decrease in the depth of the condensate river, because it increased the assisting gravitational force toward the flow direction. Furthermore, the increase in the inclination angle changed the flow regime from stratified flow to stratified-wavy. This can be clearly distinguished in figures 14(b) and 14(c) by focusing on the contours of velocity in the condensate river (the bottom part of the channel), as well as on the exit of some droplets over the liquid-vapour interface. The contours of velocity for different angles showed that, for β = 0.3°, the velocity of the condensate river was very low. However, for β = 30° and β = 60°, the

velocity increased due to the assisting gravity force, and consequently caused a decrease in the depth of the condensate river.

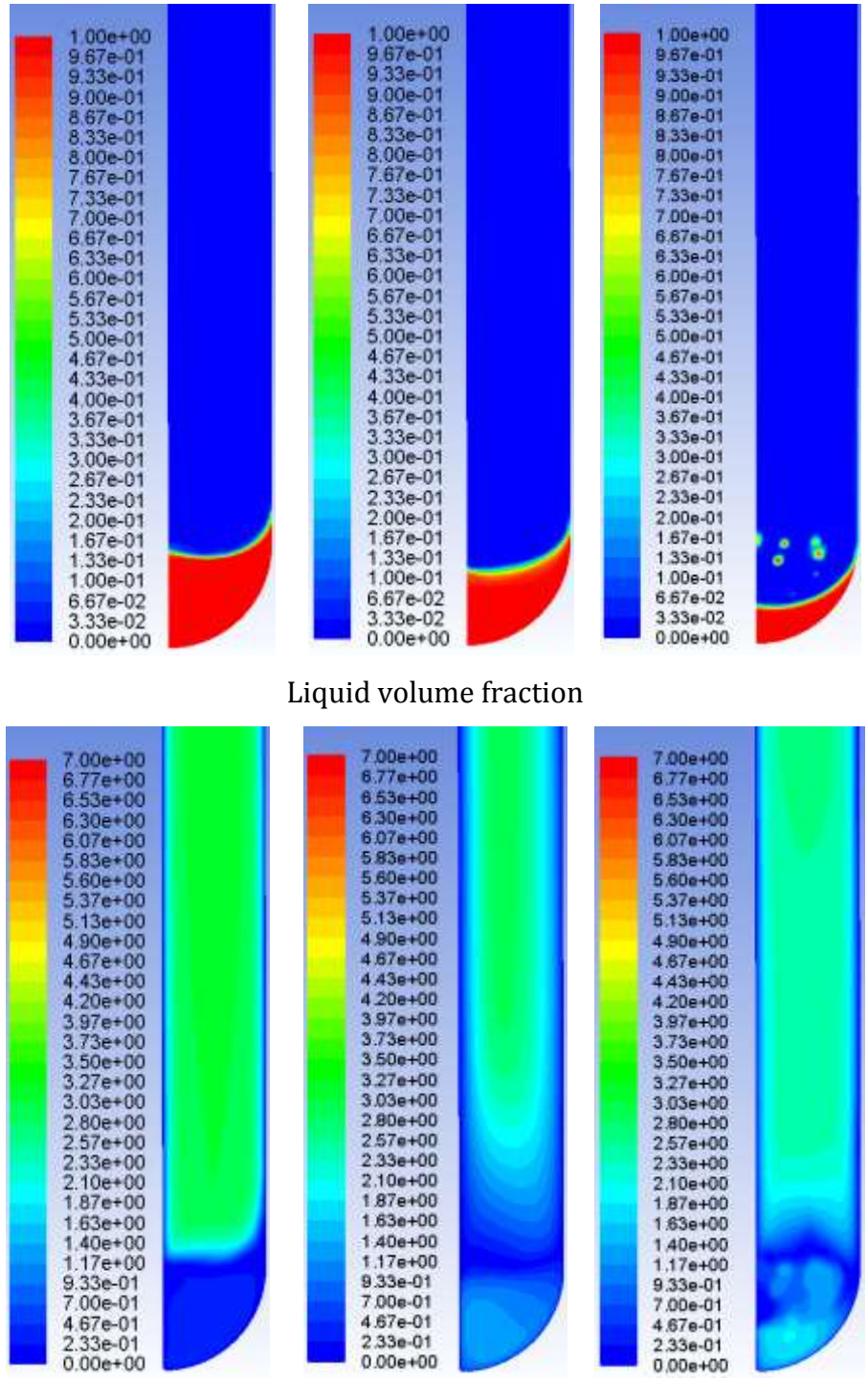

Figure 14. Variations of volume fraction and velocity at different inclination angle for G = 6.5 kg/m^{2}s and T_{sat} = 100 °C: (a) β = 0.3°; (b) β = 30°; and (c) β = 60°.

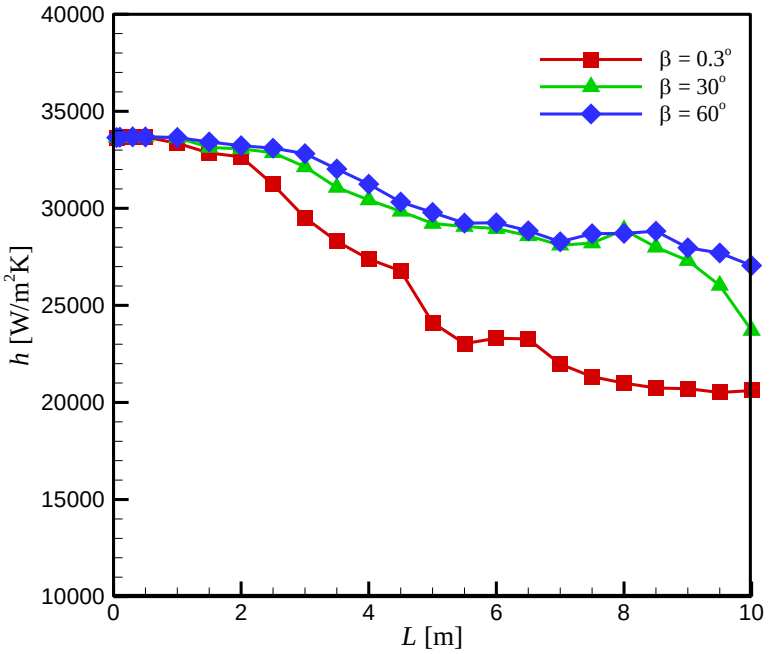

(a)

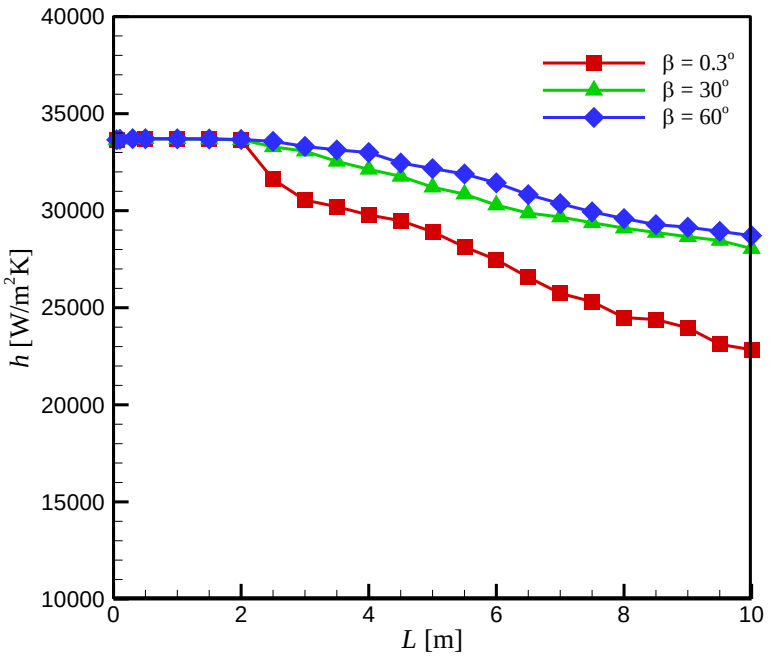

(b)

Figure 15. Effect of inclination angle on the condensation heat transfer coefficient at T_{sat} = 100 °C: (a) G = 6.5 kg/m²s; and (b) G = 10.5 kg/m²s.

The effect of inclination angle on the condensation heat transfer coefficient is illustrated in Figure 15. The results are presented for G = 6.5 kg/m^{2}s and T_{sat} = 100 °C and at different inclination angles. The effect of the inclination angle on the condensation heat transfer coefficient can be interpreted by referring to the changes in the depth of the condensate river. As discussed in Figure 14, the increase in the inclination angle decreased the condensate river depth and increased the convection effect. Both effects caused an increase in the condensation heat transfer coefficient. This effect can be clearly seen in Figures 15(a) and 15(b) for different inclination angles and steam mass fluxes. The results also show that the effect of the inclination on the condensation heat transfer coefficient was more considerable at lower inclination angles. This could be due to the fact that the increase in the convection by increasing the inclination angle was higher at lower inclination angles. At β = 0° there was no buoyancy source term in the momentum equations, but the corresponding buoyancy source terms were very high compared to the other terms in the momentum equations for both cases β = 30° and β = 60°. Therefore the increase in the convection was not considerable from β = 30° to β = 60°, and as a result the corresponding heat transfer coefficients would be almost the same for these two inclinations. Such results were also obtained for the condensation of R134a inside an inclined tube. Another point is that the effect of the inclination angle on the condensation transfer coefficient was more significant at lower steam mass fluxes, because at higher steam mass fluxes, the viscous force was dominant compared to the gravitational force.

The effect of the inclination angle on the pressure along the channel is depicted in Figure 16 for G = 6.5 kg/m^{2}s and T_{sat} = 100 °C. The results show that the inclination angle had no significant effect on the pressure along the channel length. This could be due to the fact that, at the considered operating conditions, the flow regimes did not change when the inclination angle changed. Nevertheless, the plots showed that there was a slight decrease in the pressure drop when the inclination angle increased, and this decrease was more considerable at lower steam mass fluxes.

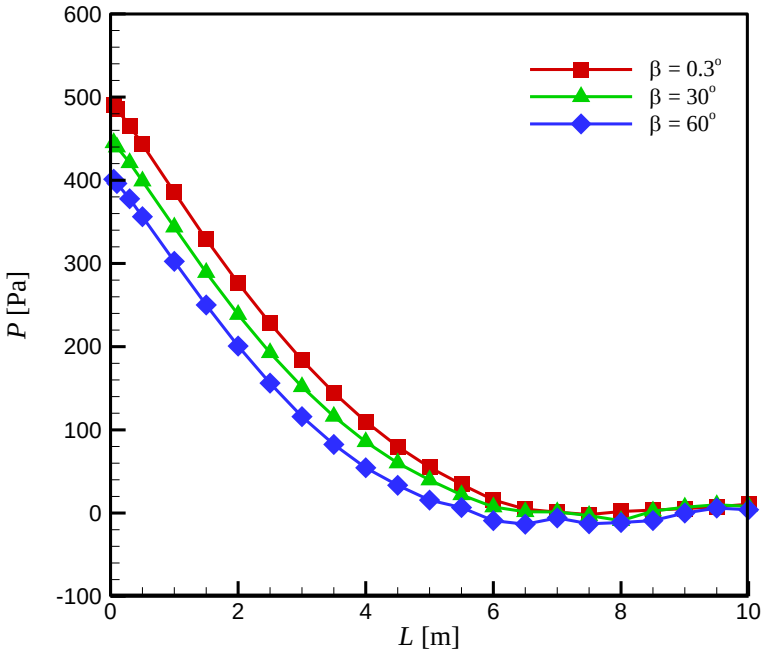

(a)

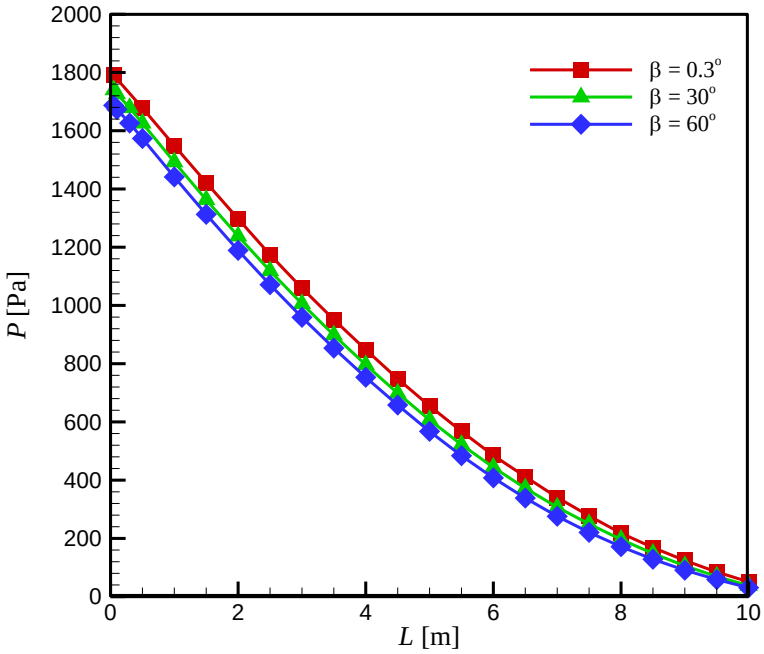

(b)

Figure 16. Effect of inclination angle on the pressure along the channel at T_{sat} = 100 °C: (a) G = 6.5 kg/m²s; and (b) G = 10.5 kg/m²s.

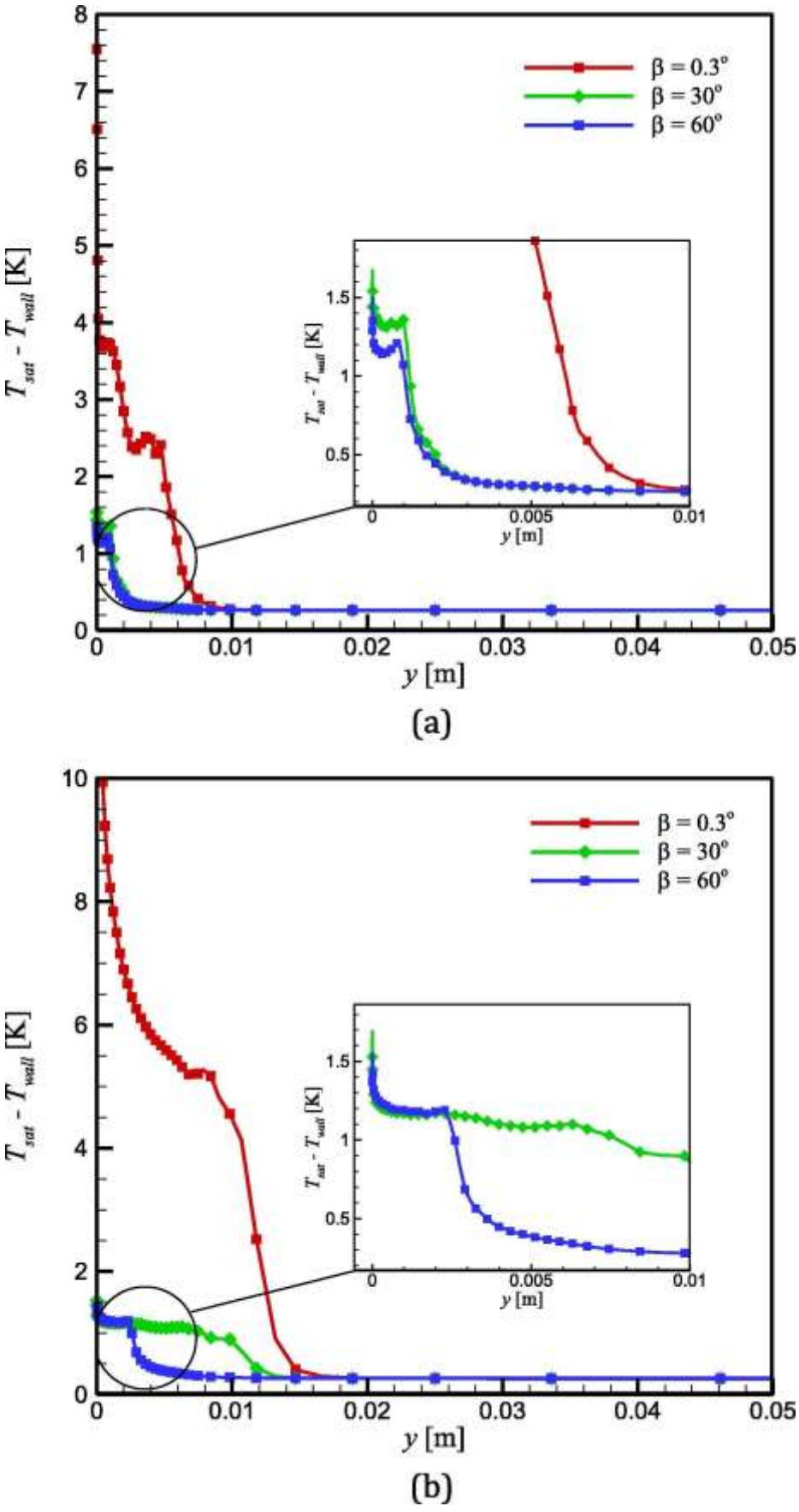

Figure 17. Effect of inclination angle on the cooling wall temperature for G = 6.5 kg/m²s and T_{sat} = 100 °C: (a) x = 6 m; and (b) x = 10 m.

Figure 17 shows the effect of inclination angle on the distribution of the cooling wall temperature at two different sections of x = 6 m and x = 10 m for G = 6.5 kg/m^{2}s and T_{sat} = 100 °C. The cooling wall temperature was lowest at the bottom region of the channel and increased rapidly along the y-coordinate. At the condensate river, due to the high thermal resistance toward the heat flux, the heat transfer coefficients and consequently the condensation rates were very low. Therefore, the heat flux caused a decrease in the cooling wall and condensate river temperatures. The results also showed that the temperature of the cooling wall was almost equal to the saturation temperature for the region outside the condensate river. As discussed before, in this region, the condensation mechanism was drop-wise, and as a result, the liquid film thickness was almost zero. The results for x = 6 m show that, with the increase in inclination angle, the temperature of the cooling wall increased considerably. The increase was more significant when the inclination angle changed from β = 0.3° to β = 30°, because at β = 0.3°, the convection in the condensate river was very low. At x = 10 m, the depth of the condensate river was higher compared to that for x = 6 m due to the condensation process. Therefore, as expected, the temperature of the cooling wall would be lower.

5.4. Effect of steam mass flux

The variations of the liquid volume fraction at the outlet region of the channel for different steam fluxes, inclination and T_{sat} = 100 °C are illustrated in Figure 18. As discussed before, the cooling wall was assumed to be a wetting surface. Therefore, the liquid-vapour interface stretched upwards, while, for the interface, it was almost perpendicular to the non-cooling wall (non-wetting surface). The contours of the liquid volume fraction for β = 30° showed that the depth of the condensate river decreased when the steam mass flux increased. This could be due to the fact that the increase in the steam mass flux caused an increase in the convection effect in both the vapour and the liquid phases. Similar trends could be seen for β = 30°, but the depth of the condensate river was lower. In the case of β = 30°, the assisting gravity force enhanced the convection effect in the condensate river due to its higher density, and as a result, the condensate river depth decreased.

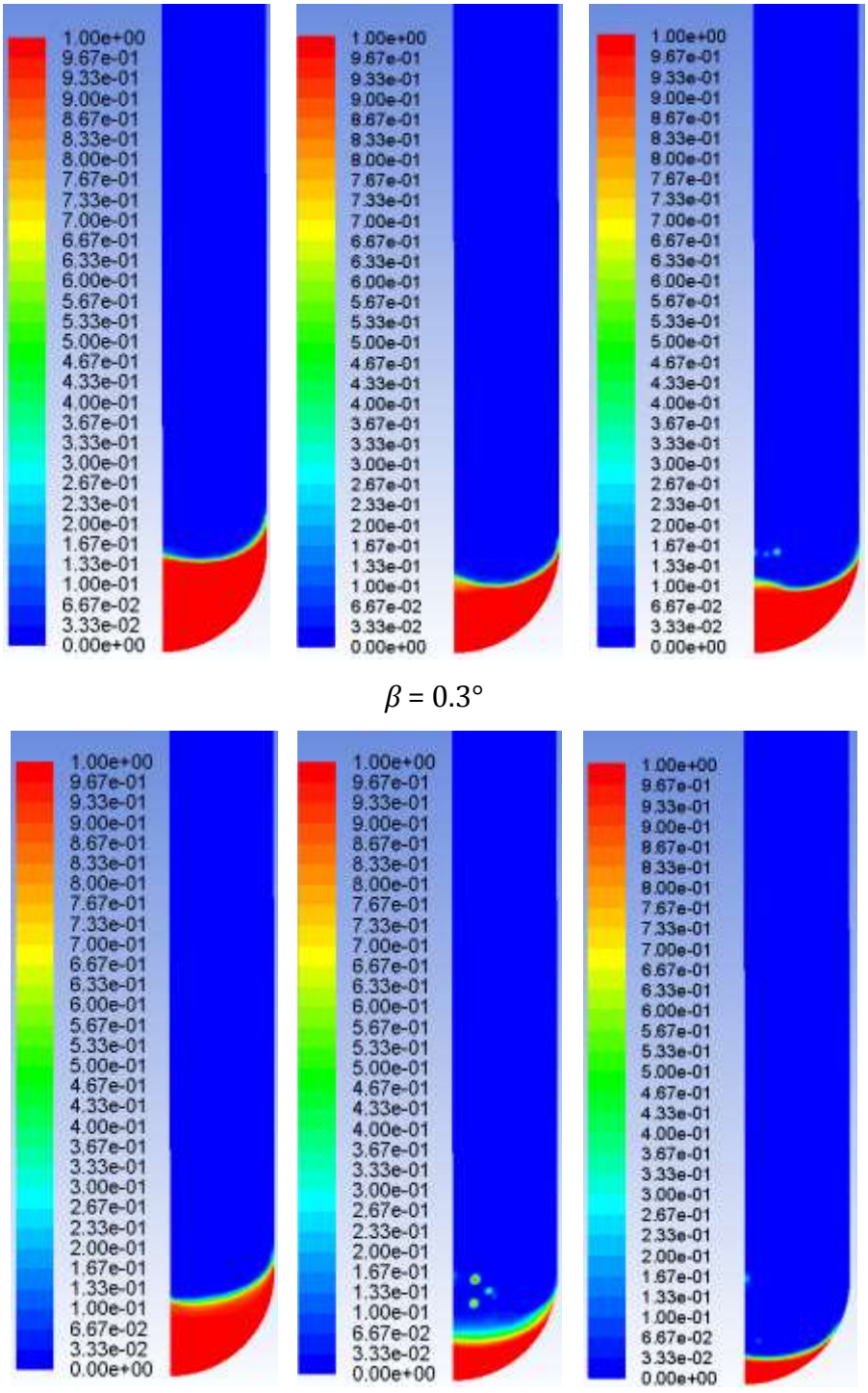

Figure 18. Effect of steam mass flux on the liquid volume fraction at T_{sat} = 100 °C: (a) G = 6.5 kg/m²s; (b) G = 8.5 kg/m²s; and (c) G = 10.5 kg/m²s.

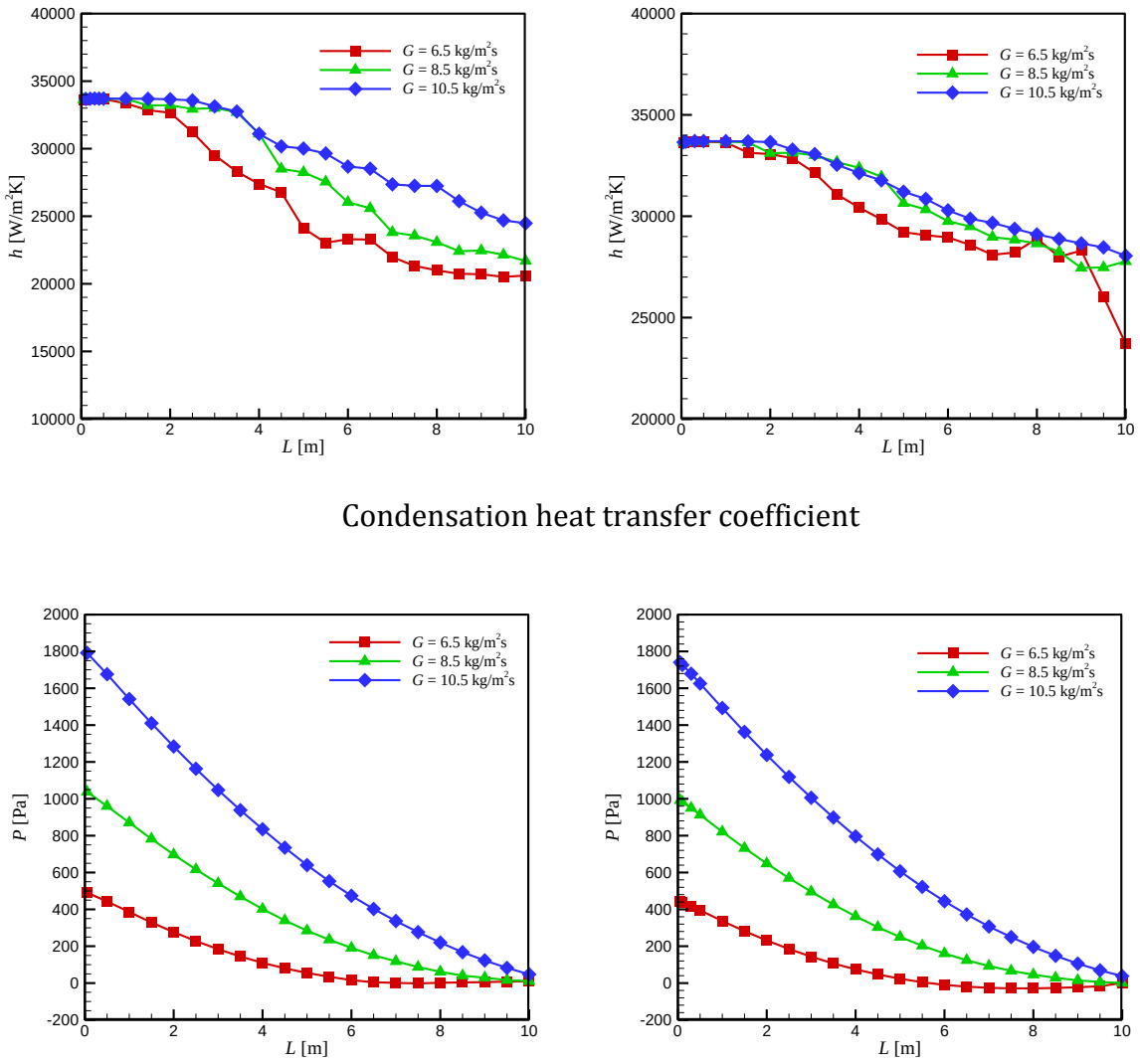

Figure 19. Effect of steam mass flux on the condensation heat transfer coefficient and pressure along the channel at T_{sat} = 100 °C: (a) β = 0.3°; and (b) β = 30°.

Figure 19 shows the effect of steam mass flux on the condensation heat transfer coefficient and pressure for two inclination angles of β = 0.3° and β = 30°, and at T_{sat} = 100 °C. As discussed before, the condensation heat transfer coefficient decreased along the channel length due to an increase in the condensate river depth and the convection decreased in the vapour phase due to the mass transfer. The results also show that the increase in the steam mass flux increased the condensation heat transfer coefficient, because it enhanced the convection effect inside the channel and also decreased the depth of the condensation river. This enhancement was more considerable when β =

0.3°, because at this condition, there was no gravity assisting force. The only reason for increasing the convection effect was the increase in the steam mass flux. The plots for the pressure distributions along the channel show that the increase in the steam mass flux increased pressure drop along the channel due to an increase in the convection effect and consequently viscose force. Another point was that the pressure dropped a little more for β = 0.3° compared to that for β = 30°.

The variations of the temperature difference between the cooling wall and saturation temperature for different steam mass fluxes, β = 0.3° and T_{sat} = 100 °C are shown in Figure 20. The results for x = 6 m show that the temperature of the cooling wall increased along the y-coordinate due to the decrease in the condensate river depth. Furthermore, it can be observed that the temperature of the cooling wall increased as the steam mass flux increased. This can be attributed to the increase in the convection effect inside the condensate river at higher steam mass fluxes, which caused the lower depth and consequently the lower thermal resistance toward the heat flux. A similar trend was seen for x = 10 m, but due to the higher condensate river depth as a result of condensation process, the temperature of the cooling wall at this section was lower than that of x = 6 m. These results further confirmed that the condensation heat transfer coefficient decreased along the channel length due to an increase in the condensation depth.

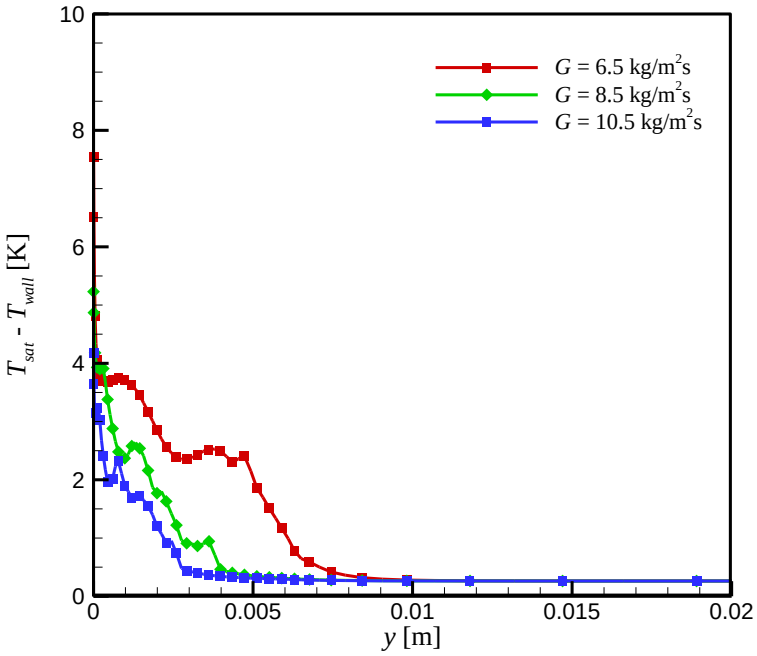

(a)

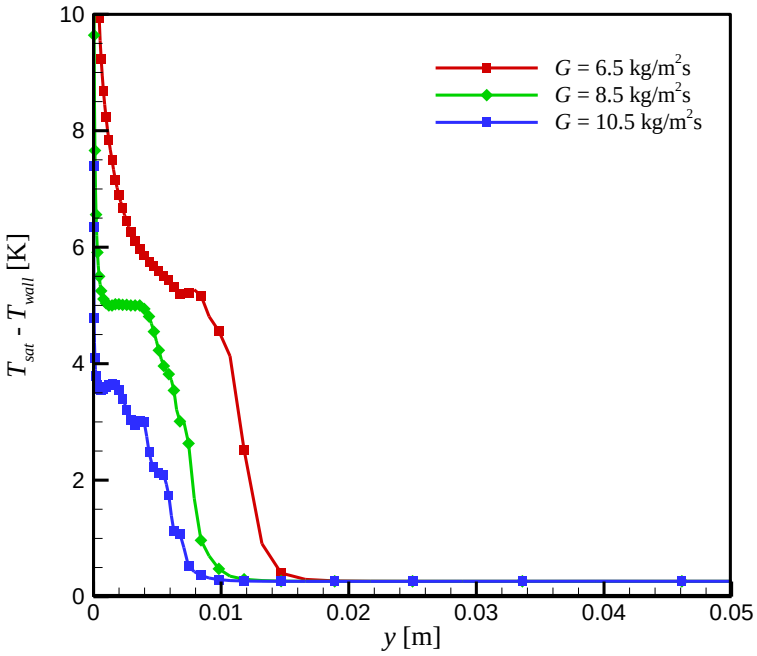

(b)

Figure 20. Effect of steam mass flux on the cooling wall temperature for β = 0.3° and T_{sat} = 100 °C: (a) x = 6 m; and (b) x = 10 m.

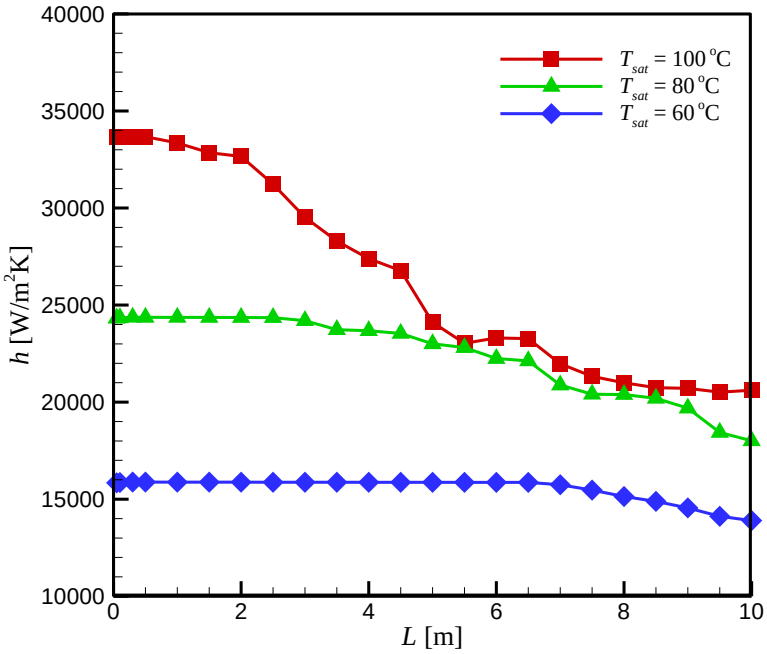

(a)

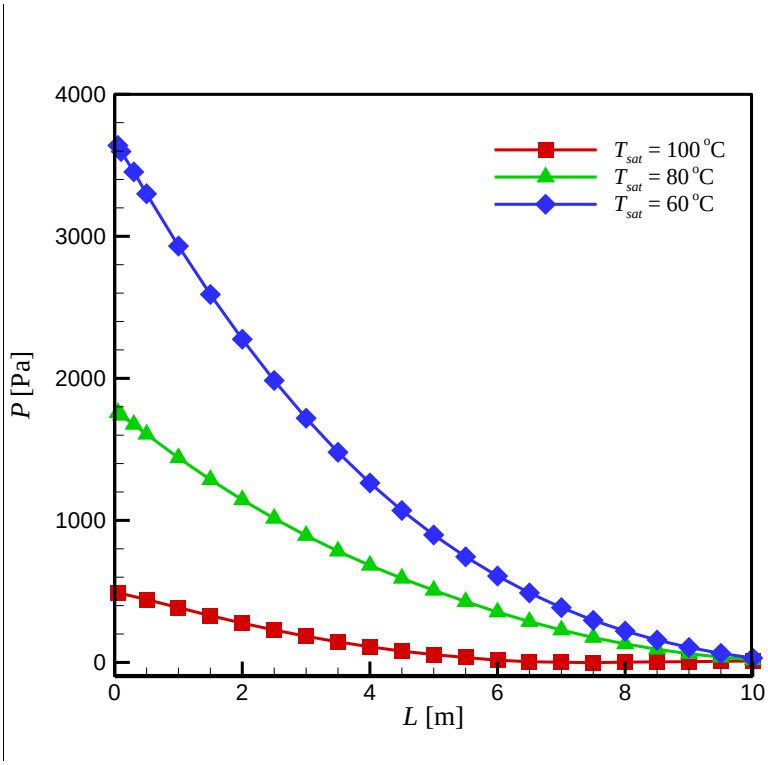

(b)

Figure 21. Effect of saturation temperature on the condensation heat transfer coefficient and pressure along the channel for $\beta = 0.3°$ and $G = 6.5$ kg/m² s: (a) condensation heat transfer coefficient; and (b) pressure.

5.5. Effect of saturation temperature

Figure 21 shows the effect of saturation temperature on the condensation heat transfer coefficient and pressure distribution along the channel for β = 0.3° and G = 6.5 kg/m^{2}s. The results clearly show that the increase in the saturation temperature caused a significant increase in the heat transfer coefficient. This could be partially due to the fact that, with the increase in the saturation temperature, the thermal conductivities of both liquid and vapour phases, which have dominant roles in the drop-wise condensation mode, increased. Furthermore, the decrease in the condensation heat transfer coefficient along the channel length became less considerable as the saturation temperature decreased, because the velocity of the steam, as well as the convection in the condensate river, which caused a decrease in its depth, were higher for the lower saturation temperatures. Another reason might be the complete condensation of steam for the case β = 0.3°, G = 6.5 kg/m^{2}s and T_{sat} = 100 °C. Another point is that, with the increase in saturation temperature, the pressure drop along the channel decreased (Figure 21(b)). This can be justified by referring to the kinematic viscosities of the liquid and vapour phases, which both decreased as the saturation temperature increased.

The variations of the temperature difference between the cooling wall and saturation temperature for β = 0.3°, G = 6.5 kg/m^{2}s, and for different saturation temperatures are shown in Figure 22. The results show two distinct regions. The first one is inside the condensate river and the other one is the surface of the cooling wall. The temperature difference inside the condensate river increased as the saturation temperature increased, because at higher saturation temperatures, the depth of the condensate river was more than that of the lower saturation temperatures, which consequently caused more thermal resistance toward the heat flux. In the region outside the condensate river, the temperature difference decreased when the saturation temperature increased. This could be due to the fact that, at higher saturation temperatures, the thermal conductivities of both liquid and vapour phases increased and caused a decrease in the thermal resistance toward the heat flux. The results for x = 6 m and x = 10 m were similar in trend, but were different in the magnitudes of the temperature difference. At x = 10 m, the temperature difference was larger, because the depth of the condensate river was higher due to the condensation phenomenon.

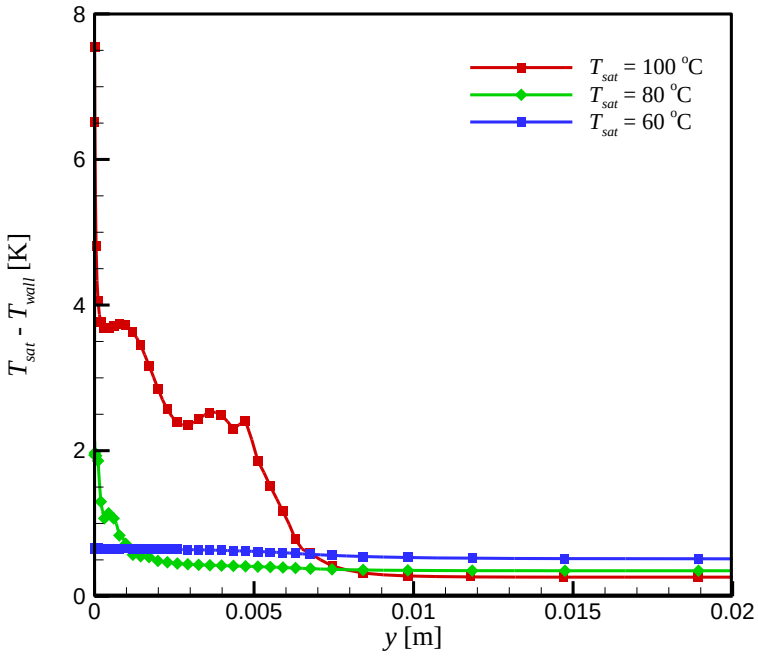

(a)

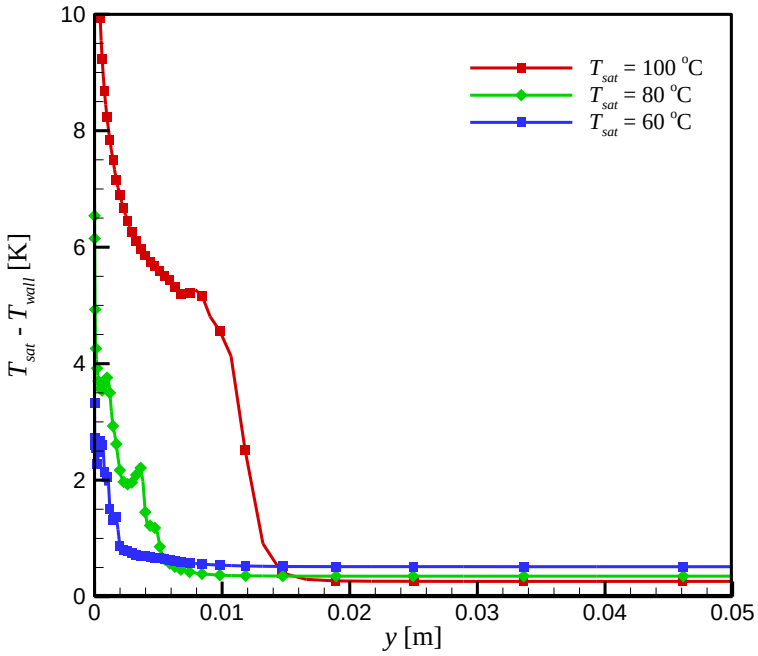

(b)

Figure 22. Effect of saturation temperature on temperature difference between the cooling wall and saturation temperature for β = 0.3° and G = 6.5 kg/m²s: (a) x = 6 m; and (b) x = 10 m.

6. Conclusion

This study was a complementary work to the previous experimental research regarding the condensation of steam inside a long, inclined flattened channel with a very high aspect ratio. In this work, using the capabilities of the CFD method, numerical simulations were performed to further investigate the problem. To do so, the VOF multiphase flow formulation was utilised to present the governing equations, as well as the dominant forces. The effects of the main flow-field parameters, such as steam mass flux, saturation temperature and channel inclination angle on the condensation phenomenon were studied. The present numerical results were in good agreement with the measured data of the previous experimental work. The following conclusions were made based on the simulation results:

I. The increase in the inclination angle, steam mass flux and saturation temperature caused an increase in the heat transfer coefficient.

II. Although the main mechanism of the condensation was drop-wise on the cooling wall, the increase in the inclination angle increased the velocity of the condensate river, which had two effects: decreasing the depth and increasing the convective heat transfer of the river. Both effects caused an increase in the heat transfer coefficient.

III. Since the void fraction was very high throughout the condenser, the increase in void fraction due to increased inclination angle did not have a significant effect on the pressure drop along the channel.

IV. The simulation showed that, at vacuum pressures, the effect of the condensate river on heat transfer coefficient decreased, and pressure drop increased significantly.

V. Finally, it was concluded that the performance of the κ-ω sst turbulence model was better than the κ-ε model. This could be due to the fact that, except at the entrance region of the channel, the flow field Reynolds numbers were low.

The results presented in this study clearly showed that the design of air-cooled heat exchangers can be logically performed in order to improve the overall performance of the device without any significant additional cost. Another point is that the simulation can be extended to other operating conditions as well as other working fluids. This capabilty is very important in an economical point of view, because it reduces the required cost and time to obtain the desired design and performance.

ACKNOWLEDGEMENT

The support and resources of the Cape Town High Performance Centre (CHPC), the Air Conditioning and Refrigeration Center at the University of Illinois, and Creative Thermal Solutions, Inc. are gratefully acknowledged.

References

[1] J.-S. Chiou, S.-A. Yang, C.o.-K. Chen, Laminar film condensation inside a horizontal elliptical tube, Appllied Mathematical Modelling, 18 (1994) 340-346.
[2] C.o.-K. Chen, S.-A. Yang, Laminar film condensation inside a horizontal elliptical tube with variable wall temperature, International Journal of Heat and Fluid Flow, 15 (1994) 75-78.
[3] G.P. Fieg, W. Roetzel, Calculation of laminar film condensation in/on inclined elliptical tubes, International Journal of Heat and Mass Transfer, 37 (1994) 619-624.
[4] S. Chen, Z. Yang, Y. Duan, Y. Chen, D. Wu, Simulation of condensation flow in a rectangular microchannel, Chemical Engineering and Processing, 76 (2014) 60-69.
[5] D.D. Col, M. Bortolato, M. Azzolin, S. Bortolin, Effect of inclination during condensation inside a square cross section minichannel, International Journal of Heat and Mass Transfer, 78 (2014) 760-777.
[6] D. Jige, N. Inoue, S. Koyama, Condensation of refrigerants in a multiport tube with rectangular minichannels, International Journal of Refrigeration 67 (2016) 202-213.
[7] Y. Kang, W.A. Davies, P. Hrnjak, A.M. Jacobi, Effect of inclination on pressure drop and flow regimes in large flattened-tube steam condensers, Applied Thermal Engineering, 123 (2017) 498-513.
[8] N.H. Kim, E.J. Lee, H.W. Byun, Condensation heat transfer and pressure drop in flattened smooth tubes having different aspect ratios, Experimental Thermal and Fluid Science, 46 (2013) 245-253.
[9] M. Darzi, M.A. Akhavan-Behabadi, M.K. Sadoughi, P. Razi, Experimental study of horizontal flattened tubes performance on condensation of R600a vapor, International Communications in Heat and Mass Transfer, 62 (2015) 18-25.
[10] T. Klahm, H. Auracher, F. Ziegler, Heat transfer during reflux condensation of an R134a/R123 mixture in vertical and inclined narrow tubular and rectangular channels, International Journal of Refrigeration, 33 (2010) 1319-1326.
[11] K. Wilber, J. Maulbetsch, Air-Cooled Condenser Design, Specification, and Operation Guidelines, EPRI, Palo Alto, CA2005, (2005).
[12] W. Li, J. Zhang, G. Bai, J.-l. Xu, T.W. Simon, J. Li, J.-j. Wei, Numerical Simulation of Condensation for R410A in Horizontal Round and Flattened Minichannels, Journal of Heat Transfer, 139 (2016) 021501.
[13] J. Wen, X. Gu, S. Wang, Y. Li, J. Tu, Numerical investigation on condensation heat transfer and pressure drop characteristics of R134a in horizontal flattened tubes, International Journal of Refrigeration, 85 (2018) 441-461.
[14] J. Zhang, W. Li, S.A. Sherif, A numerical study of condensation heat transfer and pressure drop in horizontal round and flattened minichannels, International Journal of Thermal Sciences, 106 (2016) 80-93.
[15] J. Kaew-On, N. Naphattharanun, R. Binmud, S. Wongwises, Condensation heat transfer characteristics of R134a flowing inside mini circular and flattened tubes, International Journal of Heat and Mass Transfer, 102 (2016) 86-97.
[16] S.P. Olivier, J.P. Meyer, M.D. Paepe, K.D. Kerpel, The influence of inclination angle on void fraction and heat transfer during condensation inside a smooth tube, International Journal of Multiphase Flow, 80 (2016) 1-14.

[17] A.K. Solanki, R. Kumar, Condensation of R-134a inside micro-fin helical coiled tube-in-shell type heat exchanger, Experimental Thermal and Fluid Science, 93 (2018) 344-355.
[18] D.J. Kukulka, R. Smith, W. Li, Comparison of tubeside condensation and evaporation characteristics of smooth and enhanced heat transfer 1EHT tubes, Applied Thermal Engineering, 89 (2015) 1079-1086.
[19] M. Darzi, M.K. Sadoughi, M. Sheikholeslami, Condensation of nano-refrigerant inside a horizontal tube, Physica B: Condensed Matter, 537 (2018) 33-39.
[20] A.O. Adelaja, J. Dirker, J.P. Meyer, Experimental study of the pressure drop during condensation in an inclined smooth tube at different saturation temperatures, International Journal of Heat and Mass Transfer, 105 (2017) 237-251.
[21] S. Lips, J.P. Meyer, Experimental study of convective condensation in an inclined smooth tube. Part II: Inclination effect on pressure drops and void fractions, International Journal of Heat and Mass Transfer, 55 (2012) 405-412.
[22] S. Lips, J.P. Meyer, Experimental study of convective condensation in an inclined smooth tube. Part I: Inclination effect on flow pattern and heat transfer coefficient, International Journal of Heat and Mass Transfer, 55 (2012) 395-404.
[23] J.P. Meyer, J. Dirker, A.O. Adelaja, Condensation heat transfer in smooth inclined tubes for R134a at different saturation temperatures, International Journal of Heat and Mass Transfer, 70 (2014) 515-525.
[24] S.M.A.N.R. Abadi, J.P. Meyer, J. Dirker, Numerical investigation of condensation inside an inclined smooth tube, in: Proc. 13th Int. Conf. Heat Transfer, Fluid Mechanics and Thermodynamics, Portoroz, Slovenia, 2017, pp. 576-572.
[25] S.M.A.N.R. Abadi, J.P. Meyer, J. Dirker, Effect of inclination angle on the condensation of R134a inside an inclined smooth tube, Chemical Engineering Research and Design, 132 (2018) 346-357.
[26] S.M.A.N.R. Abadi, J.P. Meyer, J. Dirker, Numerical simulation of condensation inside inclined smooth tube, Chemical Engineering Science, 182 (2018) 132–145.
[27] S.M.A.N.R. Abadi, J.P. Meyer, Numerical investigation into the inclination effect on conjugate pool boiling and the condensation of steam in a passive heat removal system, International Journal of Heat and Mass Transfer, 122 (2018) 1366-1382.
[28] K. Kekaula, Y. Chen, T. Ma, Q.-W. Wang, Numerical investigation of condensation in inclined tube air-cooled condensers, Applied Thermal Engineering, 118 (2017) 418-429.
[29] P.D. Schoenfeld, D.G. Kröger, Flooding during reflux condensation of steam in an elliptical tube, R & D Journal, 16 (2000).
[30] M. Owen, D.G. Kröger, A numerical investigation of vapor flow in large air-cooled condensers, Applied Thermal Engineering, 127 (2017) 157-164.
[31] Y. Kang, W.A. Davies, P. Hrnjak, A.M. Jacobi, Effect of Inclination on Pressure Drop in Large Flatened-Tube Steam Condensers, in: 16th International Refrigeration and Air Conditioning Conference at Purdue, July 11-14, 2016, 2016.
[32] W.A. Davies III, Y. Kang, P. Hrnjak, A.M. Jacobi, Heat transfer and flow regimes in large flattened-tube steam condensers, Appl. Therm. Eng., (2018).
[33] W.A. Davies, Y. Kang, P. Hrnjak, A.M. Jacobi, Method for evaluating the effect of inclination on the performance of large flattened-tube steam condensers with visualization of flow regimes, Applied Thermal Engineering, 138 (2018) 934-941.
[34] T. Cheng, X. Du, L. Yang, Y. Yang, Co-current Condensation in an Inclined Air-cooled Flat Tube with Fins, Energy Procedia, 75 (2015) 3154 - 3161.
[35] S.M.A.N.R. Abadi, M. Mehrabi, J.P. Meyer, Numerical study of steam condensation inside a long, inclined, smooth tube at different saturation temperatures, International Journal of Heat and Mass Transfer, 126, Part B (2018) 15-25.
[36] C.W. Hirt, B.D. Nichols, Volume of fluid (VOF) method for the dynamics of free boundaries, Journal of Computional Physics 39 (1981) 201-225.

[37] J.U. Brackbill, D.B. Kothe, C. Zemach, A continuum method for modeling surface tension, Journal of Computional Physics, 100 (1992) 335-354.
[38] F.R. Menter, Two-Equation Eddy-Viscosity Turbulence Models for Engineering Applications, AIAA Journal, 32 (1994) 1598-1605.
[39] Z. Z. Yang, T.H. Shih, New time scale based k-ε model for near wall turbulence, AIAA Journal, 317 (1993) 1191-1197.
[40] W.H. Lee, A pressure iteration scheme for two-phase flow modeling, Multiphase Transport Fundamentals, Reactor Safety, Application, 1 (1980) 407-431.
[41] Q. Shen, D. Sun, S. Su, T.J. Ning Zhang, Development of heat and mass transfer model for condensation, International Communications in Heat and Mass Transfer, 84 (2017) 35-40.
[42] W.A. Davies, P. Hrnjak, Effects of airflow direction, air velocity profile, and condensation pressure on the performance of air-cooled condensers, in: 17th International Refrigeration and Air Conditioning Conference, Purdue University, July 9-12, 2018.
[43] W.A. Davies, P. Hrnjak, Thermo-hydraulic model for steam condensation in a large, inclined, flattened-tube air-cooled condenser, in: 17th International Refrigeration and Air Conditioning Conference, Purdue University, July 9-12, 2018.
[44] P.A. Lockhart, R.C. Martinelli, Proposed correlation of data for isothermal two-phase two-component flow in pipes, Chemical Engineering Progress, 45 (1949) 39-48.